Heliyon 10 (2024) e26283

Contents lists available at ScienceDirect

Heliyon

journal homepage: www.cell.com/heliyon

Research article

Three dimensional analysis of the exhalation flow in the proximity of the mouth

F.A. Berlanga [a,*], P. Gomez [a], A. Esteban [a], L. Liu [b], P.V. Nielsen [c]

[a] Dept. de Mecánica, ETSII, Universidad Nacional de Educación a Distancia (UNED), E-28040, Madrid, Spain
[b] Dept. of Building Science and Technology, School of Architecture, Tsinghua University, Haidian District, Beijing, China
[c] Dept. of the Built Environment, Aalborg Universitet, Thomas Manns Vej 23 9220 Aalborg Øst, Denmark

ARTICLE INFO

Keywords:
Cross infection risk
Turbulent jet
Exhalation flows
Realistic model

ABSTRACT

The human exhalation flow is characterized in this work from the three-dimensional velocimetry results obtained by using the stereo particle image velocimetry (SPIV) measurement technique on the flow emitted from a realistic airway model. For this purpose, the transient exhalation flow through the mouth of a person performing two different breaths corresponding to two metabolic rates, standing relaxed (SR) and walking active (WA), is emulated and studied. To reproduce the flow realistically, a detailed three-dimensional model obtained from computed tomography measurements on real subjects is used. To cope with the variability of the experimental data, a subsequent analysis of the results is performed using the TR-PIV (time resolved particle image velocimetry) technique. Exhalation produces a transient jet that becomes a puff when flow emission ends. Three-dimensional vector fields of the jet velocity are obtained in five equally spaced transverse planes up to a distance of 50 mm from the mouth at equally spaced time instants (0.125 s) which will be referred to as phases (φ), from the beginning to the end of exhalation. The time evolution during exhalation of the jet area of influence, the velocity field and the jet air entrainment have been characterized for each of the jet cross sections. The importance of the use of realistic airway models for the study of this type of flow and the influence of the metabolic rate on its development are also analyzed. The results obtained contribute to the characterization of the human exhalation as a pathway of the transmission of pathogens such as SARS-CoV-2 virus.

1. Introduction

The air flow generated by human exhalation is saturated and carries droplets in the form of aerosols that may contain infectious pathogens, and is therefore considered one of the main sources of infectious diseases [1–3]. The flow of emitted droplets have been extensively studied [4–11]. It has been characterized by variables such as the total number of droplets, their size distribution, the velocity of emission, and the distance they travel, which depend on the type of respiratory phenomenon that transports them, such as coughing, sneezing, breathing or speaking, and on other factors associated with the physical characteristics of the individual, ambient conditions and the exhalation generation process itself [5,8,12]. A large number of droplets of very different sizes (1 μm to 1 mm) are produced in each exhalation [13].

* Corresponding author.
E-mail addresses: felixberlanga@ind.uned.es (F.A. Berlanga), pgomez@ind.uned.es (P. Gomez), aesteban@ind.uned.es (A. Esteban), liuli_archi@tsinghua.edu.cn (L. Liu), pvn@civil.aau.dks (P.V. Nielsen).

https://doi.org/10.1016/j.heliyon.2024.e26283
Received 1 August 2023; Received in revised form 2 February 2024; Accepted 9 February 2024
Available online 15 February 2024

Once the droplets are emitted from the airways, an evaporation process begins, the rate of which depends on environmental conditions such as relative humidity and temperature [8,10,14]. Large droplets follow a parabolic trajectory due to the effect of gravity and fall to the ground before evaporating. These droplets result in the first path or mode of pathogens transmission, which occurs when another individual is close enough for the ejected droplets to reach him or her before falling to the ground. Droplets falling to the ground lead to a contaminated surface known as fomite, which may result in a second route of transmission, occurring by direct contact with the secretion [15]. On the other hand, the small droplets, due to the evaporation process, lose volume until they are reduced to a solid residue, with a typical size of less than 5-10 μm [8,13,14,16], also known as droplet nuclei, which contains the pathogens and remains suspended in the air forming an aerosol, which is entrained by the air and can reach long distances from the source, resulting in the third transmission route, which, unlike the previous two, is considered to be long-range. The limit for airborne particles is not entirely clear, since there are other factors related to the characteristics of the expiratory flow and the surrounding ambient, such as the momentum and the intensity of the turbulence in the expiratory flow or relative humidity, which may influence the ability of particles to remain suspended [17,18]. For given ambient conditions and exhalation height, there is a critical size of the ejected droplet above which the droplet falls to the ground and below which it evaporates completely and remains suspended. Wells [19] studied the time taken by droplets of different sizes emitted on exhalation to evaporate and proposed a first droplet evaporation-fall graph that has been widely used, in which the evaporation and fall times are plotted together as a function of droplet size, along with the cut-off point of the two curves determining the critical size. Wells obtained a critical size value of 100 μm for a height of 2 m, considering that this value determines the boundary between the so-called large and small droplets, which will lead to droplet nuclei or aerosol formation. This critical value has subsequently been widely accepted [14,16,17]. Other later studies have studied the influence of various factors, such as, for example, relative humidity [8], whose increase causes the critical size to decrease since it increases evaporation times, or the effect of different respiratory phenomena [9].

In the case of SARS, the two short-range routes of infection have traditionally been considered the predominant ones, which led interest to focus initially on the study of the distribution and evolution of ejected droplets [6,8,14,20]. However, during the COVID-19 pandemic, it became clear that these two routes could not be responsible for such a high volume of infections, taking into account, in addition, the infection control measures that were being applied based, among other means, on the use of surgical masks, reducing direct contact, cleaning surfaces and maintaining a physical distance [21]. Different studies have demonstrated the importance of airborne transmission, even considering it as the dominant route of transmission [17,21–23]. The World Health Organization (WHO) changed its point of view and officially acknowledged that the airborne transmission is a main transmission mode in spreading COVID-19 at both short and long ranges in 2021 [23]. This has highlighted the need to implement other types of measures such as ventilation or reducing exposure times in enclosed areas, and, on the other hand, also the need to better understand the characteristics of the exhalation flow that transports these small particles, of which there are relatively few studies [24].

Of the different types of exhalations, coughing [10,14,25–29] and, to a lesser extent, sneezing [12,20,24,30], are the ones that have been most extensively studied because of their high potential as sources of disease spread, since they result in violent exhalations that generate a flow with a higher velocity, and expel a greater number of droplets of different sizes, which, in turn, are transported greater distances. Speech is also recently receiving much attention since it is an exhalation that occurs at very high velocity, resulting in a turbulent flow that promotes to the formation of a large number of droplets on expiration [24,31–33]. The droplet size distribution when speaking is similar to that of coughing, although the total volume of liquid generated per liter of air is smaller [34,35]. In the case of breathing, air flow in the airways occurs at a slower rate than in the other types of exhalation, and results in less droplet generation and entrainment. The particle size and total volume of liquid produced in respiration is several orders of magnitude smaller than in coughing [36], and, although these quantities increase considerably with metabolic activity, in principle, it has not been considered a respiratory activity with a significant risk. However, these small droplets produced in respiration, given their small size, remain suspended in the air as aerosols for hours [23], and, since respiration is a continuous activity, if there is no adequate ventilation, an accumulation of suspended particles can occur, reaching levels that pose a clear risk of contagion [35]. Moreover, the incubation period of the coronavirus is very long, between 7 and 14 days [37], and only a very low percentage of infected subjects, approximately 35 % according to data collected by health authorities, have symptoms [38], which justifies that some studies have shown that asymptomatic and pre-symptomatic persons can shed SARS-CoV-2 virus at a higher rate than symptomatic individuals [39]. All the foregoing highlights the importance of studying and characterizing respiration as a potential source of infected aerosol generation.

Different experimental techniques have been used to study exhalation flow [40,41]. The first studies that have aimed at analyzing exhaled air flow rate have used spirometers as an experimental tool with real subjects (see, e.g. [29,42]), providing information to establish the respiratory flows of individuals according to their physical characteristics and metabolic activities. The exhaled flow rate in breathing can be described by a sinusoidal function over time [29]. In the cough, the volumetric flow rate is characterized by a very early peak value that is reached within a few milliseconds, after which the flow rate decreases in tenths of a second, and the total volume of air expired is higher than in breathing [29]. It was found that the values obtained in the measurements change from one subject to another depending on different factors such as age, gender or height and the experimental conditions of (see, e.g., Leiner et al. [43]). In order to delimit the area of influence of the exhalation flow and its propagation velocity, flow visualization techniques such as the Schlieren camera [44], shadowgraph [45] or particle tracking [46] have been used. These techniques have allowed to study the general evolution of the exhalation flow and to characterize them as transient jets or puffs with a typical propagation velocity of between $0.3\,\mathrm{m\,s^{-1}}$ and $1.4\,\mathrm{m\,s^{-1}}$ for breathing [45,47], between $2.2\,\mathrm{m\,s^{-1}}$ and $14\,\mathrm{m\,s^{-1}}$ for coughing [48]. In the sneeze have been obtained values similar to those of the cough have been obtained [48]. The opening angles captured vary from 30° for breathing [29], 25° for coughing to 15° for sneezing [12]. The maximum jet penetration range varies between 0.6 m and 0.8 m for different exhalation types [45]. A comprehensive compilation of results can be found in [41]. Bourouiba et al. [12] distinguished two phases in the exhalation flow for both coughing and sneezing: an initial starting turbulent jet driven by the momentum provided by the source, which evolved into a puff when the momentum and buoyancy effects became comparable. Liu et al. [49] compared the experimental results of the evolution of a transient jet of a cough and a stationary jet with the same discharge velocity, observing that the propagation velocity in the case of the transient jet is lower, but its spam-wise expansion rate is higher. Wei et al. [50] analyzed the behavior of transient water jets in similarity conditions, considering three different temporal exit velocity profiles: pulsation, sinusoidal and real cough, with the same injected fluid volume, finding that the sinusoidal and the real cough injections lead to a longer penetration length. Nevertheless, despite all the information that visualization techniques provide, they do not allow to get a precise measurement of the air velocity within the exhalation.

To analyze flow dynamics more precisely, point-wise velocity measurement techniques such as hot wire [49] and hot sphere velocimetry [44] have been used to obtain accurate velocity measurements in located positions. Since these techniques are invasive and each anemometer is only able to obtain velocity measurements for a single point, obtaining a velocity profile requires a repetitive measurement procedure.

One technique that solves the disadvantages of the point-wise measurement is two-dimensional particle image velocimetry (2D PIV), one of the most common noninvasive velocimetry techniques, which allows to obtain two dimensional velocity fields in a measurement plane [51]. Different studies have reviewed the advances of this technique and its application, among other research fields, in the study of respiratory flows [51,52]. The accuracy of this experimental technique is lower than the use of the hot wire. However, if the particle seeding is done properly, the accuracy that can be obtained is close to that of the latter. [53]. An example of the first applications of this technique to exhalation flows is the work of Zhu et al.. [54], who analyzed the cough of three subjects and presented instantaneous velocity fields with velocities ranging from 6 to $22\,\mathrm{m\,s^{-1}}$ and an average of the maximum velocity of $11.2\,\mathrm{m\,s^{-1}}$ using an $80 \times 80\,\mathrm{mm}$ measuring window placed in the vicinity of the mouth in a vertical plane that coincides with the symmetry plane, which we refer to hereafter as the longitudinal plane. Kwon et al. [55] studied cough and speech in 26 subjects, with a measurement window of $247 \times 184\,\mathrm{mm}$, presenting a sequence of the time evolution of the instantaneous velocity fields with an interval of $70\,\mathrm{ms}$ and a mean value of the maximum velocity of $15.3\,\mathrm{m\,s^{-1}}$ for males and $10.2\,\mathrm{m\,s^{-1}}$ for females, and determining the flow direction with the analysis of the vertical and horizontal velocity components. Vansciver et al. [28] used the PIV system to study the cough of 29 volunteers, obtaining average velocity profiles of the cough jet at different downstream distances from the mouth using an ensemble of the measurements at three specific instants. The velocity profiles present self-similarity at streamwise distance $x/D > 6$, but they do not correspond to a Gaussian profile. They obtained an average maximum velocity of $10.2\,\mathrm{m\,s^{-1}}$ with a standard deviation of $6.7\,\mathrm{m\,s^{-1}}$. More recently, Han et al. [24,53] registered the ensemble-averaged vertical and horizontal velocity profiles of the coughing, sneezing and speaking of several subjects. Dudalski et al. [56] studied the maximum velocity values at different distances from the mouth, comparing the cough produced by sick and healthy participants, finding insignificant differences in terms of velocity and turbulence intensity. The results obtained in the different studies showed a great variability from one individual to another, and even between exhalations from the same individual [28].

The PIV technique presents a limitation related to health hazards due to the use of laser light and tracer particles in experimentation with real subjects [41]. The use of laser light requires protective measures, such as employing, which affect the position to be adopted by the individuals, limit their metabolic activity and may disturb the flow. Moreover, it is necessary to seed the airflow with a precise concentration of particles to ensure a correct velocity measurement. It is difficult to find particles that can be exhaled directly by a person in a pressurized and controllable concentration without being harmful to its health. Moreover, if particles are added after the flow has been exhaled, the flow may be disturbed [53].

The use of manikins resembling real human subjects avoids these issues and at the same time allows to consider the effect of the body thermal plume. Marr et al. [57] and Feng et al. [58] studied exhalation flows using the PIV technique considering breathing thermal manikins with simplified airway models. Marr et al. [57] used a stereo PIV system to obtain the three velocity components in the longitudinal plane in order to study the anisotropy in the breathing flow, concluding that the results obtained suggest that the airflow due to breathing is anisotropic. Feng et al. [58] analyzed inhalation and exhalation flows in a mouth breathing process, obtaining the velocities, vorticity and turbulence intensity in a determined domain. The results obtained with the simplified breathing models yield to a self-similar bell-shaped velocity distribution that differs from that observed in the experiment with real subject. Xu et al. [44] studied the differences in breathing flow between a standard manikin and human subjects using a hot-sphere anemometer capable of measuring low and varying air velocities in the range of $0.05\,\mathrm{to}\,5\,\mathrm{m\,s^{-1}}$, air temperature and turbulence intensity. In the vicinity of the mouth, the airflow of human respiration has a more complex flow pattern, with a lower maximum velocity and a higher level of turbulence. Moreover, while the direction of flow in manikins with simplified airways is horizontal, in human subjects it suffers from deviations that depend on various factors such as the shape of the mouth or the location of the teeth. An intermediate solution is the use of models with realistic airways that can reproduce flows closer to those of a real exhalation. Geoghegan et al. [59] use two simplified 3D models of the shape that adopts articulators (lips, teeth, tongue, hard palate, and larynx) constructed from magnetic resonance imaging (MRI) while a subject is producing a fricative ‘s’ and ‘sh’ sound, and stereo PIV to analyze the flow inside the upper airways and passing to the mouth. The results showed a complex flow, far from one with uniform profiles, and shows how the shape that articulators adopt influences the flow characteristics. Berlanga et al. [60] highlighted the influence of the airways geometry of the model on the characterization of exhalation flows, comparing a simplified airway (straight circular tube ending in a semi-elliptical orifice) and a realistic 3D scanned model of the airway. The core structure of the jet turned out longer and clearer in the case of the simplified model, for which a higher propagation of the initial vortex ring was observed.

The characteristics of the cross section of the flow has received scant attention in the study of exhalation airflow. Most of the studies based on PIV have focused on the longitudinal plane, due to the bidimensional nature of the results obtained with this technique. The three-dimensional velocity distribution of exhalation has not been studied experimentally [25], and only a few

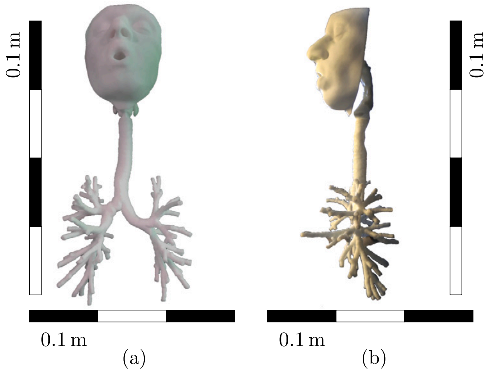

Fig. 1. Airways used for the experiments. (a) Front view, (b) Lateral view.

experimental studies have considered velocity variation in horizontal planes. Han et al. [53] used PIV to study the velocity profile in three horizontal sections, finding a spread angle similar to that obtained in the vertical direction and certain deviation of the center line from the longitudinal plane. Geoghegan et al. [59] used stereo PIV to obtain the velocity distribution in sagittal plane and in planes parallel to the transverse and coronal planes, all in the interior of upper airways, for the airflow corresponding to the pronunciation of two fricatives consonants, although outside of the mouth they only presented results in the sagittal plane.

In this work, a study of the airflow in breathing exhalation is performed using a realistic 3D scanned model of the airway and stereo PIV. This technique has allowed to measure the distribution of the three velocity components in cross sectional planes located in the proximity of the mouth and, in this way, to obtain the evolution of the velocity field distribution and turbulence intensity throughout the exhalation. From these results, it has been possible to characterize the shape of the cross section of the flow, to obtain 2D distributions of the velocity vectors in the transversal sections, to determine the evolution of the volumetric flow rate along the jet and hence the air entrainment flow rate, the centerline displacement and jet opening in both the horizontal and vertical directions, which are measured as angles in its spatial and temporal development, have also been obtained along the exhalations. In this work an experimental study of the airflow in breathing exhalation is performed in order to increase the knowledge of this potential source of pathogen transmission that has not received as much attention as other type of exhalations. It has been use a 3D scanned model of the airway, that produces more realistic exhalations than the simplified models commonly used in the literature and avoid the limitations of the experiments with human subjects, and the Stereo PIV technique to obtain three-dimensional velocity fields for the resulting flow. The experimental data collected has made it possible to determine that the jet adopts a transversal oval shape in the initial phases of the exhalation, with the distribution of velocities in the jet and the external flow entrainment being dependent on the sine shape of the function describing the emitted exhalation flow. It has also been determined that both the centerline and the jet aperture change throughout the exhalation, especially in their horizontal direction.

2. Materials and methods

2.1. Experimental facilities

To reproduce the respiratory tract of a person, a three-dimensional model of an exhalation airways is printed in SLA resin (SPR6000, Hengtong Ltd, China). The model, shown in Fig. 1(a) front side and, (b) lateral view, considers the airways from the fourth bronchial division to the point of exhalation, which in this case is the mouth. The airways model has three types of openings: nostrils, mouth and bronchi, with an exit cross-sectional area of the mouth outlet orifice of $a_0 = 260\,\mathrm{mm}^2$. To perform an exhalation, the air is introduced through the orifices located at the fourth bronchi divisions and can be exhaled through the nostrils and the mouth apertures. To avoid adding complexity to the outflow, the model has the nose orifices blocked, so air can only be exhaled through the mouth of the model. Detailed information on the airway model used can be found in Appendix A. To conduct the experiments under the desired standstill conditions, a closed, unventilated indoor room is used, in which a constant temperature of 18 ± 0.5 °C is maintained during the course of all experiments. The arrangement of the experimental components within the room can be seen in Fig. 2(a). The temperature is controlled in two different positions inside the room, S_1 and S_2, by placing probes at nine heights at each position along the total height of the room. It is tried to keep the parasitic currents inside the room as low as possible so that they would not interfere with the experimental measurements. For this purpose, the room is kept closed during the experiments and possible parasitic currents are controlled using a fog flow identifier (CH25301, Dräger, Germany). The arrangement of the experimental components, including the model, the cameras and the laser illumination system is schematically represented in Fig. 2(b). To study the exhalation flow, ensuring that the air is introduced through all the bronchi openings, the lower part of the airway (see Fig. 1), which resembles the bronchi, is introduced into a hermetically sealed chamber with only two openings. One of the openings is connected to an artificial lung that is capable of precisely reproduce the exhalations flows under study, and the other is the trachea of the airways model, as shown in Fig. 2(c). The air is hence introduced into the one chamber opening and, by the over pressure created inside driven through the bronchi orifices to the exhalation point, the mouth of the airways.

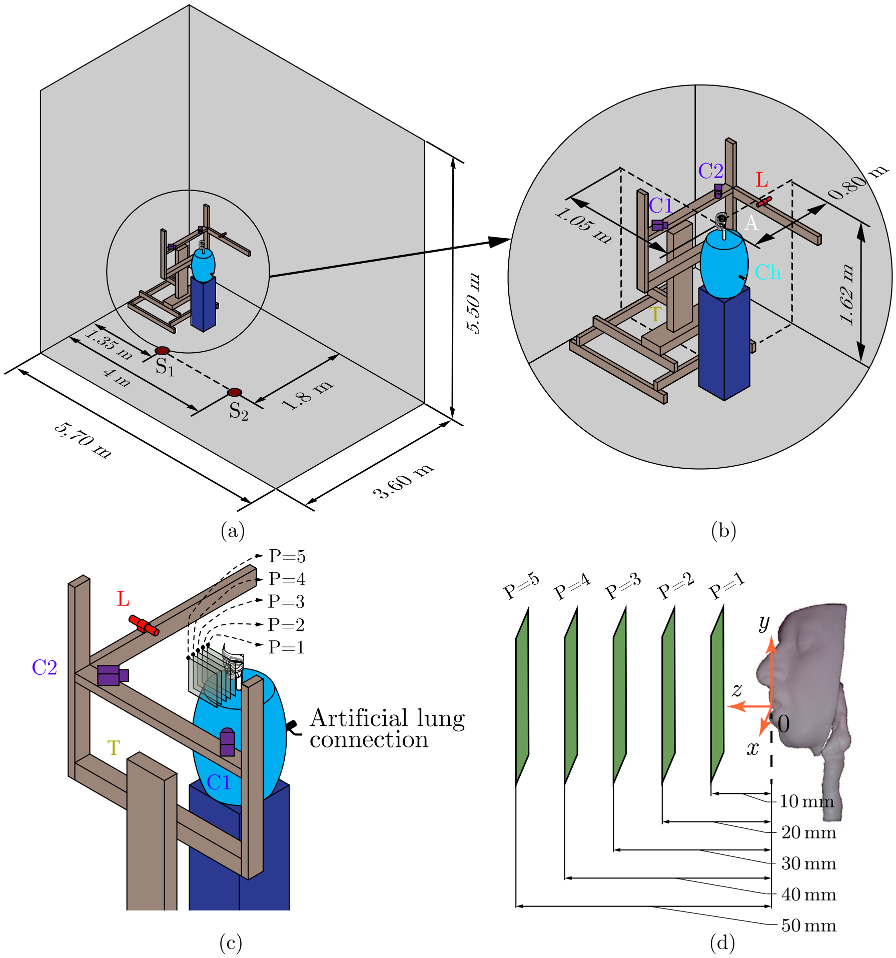

Fig. 2. Arrangement of experimental components. (a) Perspective view of the room. (b) Airways used for the experiment, A; cameras with CCD sensors of the Stereo PIV system, C1 and C2; hermetically sealed chamber, Ch; detail of the area where the experiment is performed: laser light emission optics, L. (c) Location of the measuring planes in the experimental setup. (d) Distances of the measurement planes (P = 1,2,...,5) from the mouth and Cartesian coordinate system with its origin, 0, located at the mouth.

2.2. Exhalations models

Studies carried out on human breathing have determined that the characteristics of the person and its metabolic activity determine the exhalation flow rate [29,61]. In this study, two different exhalations models are studied, each one performing a different transient respiratory flow rate. Both correspond to a woman performing different activities. One agrees with metabolic activity of 1.2 met, which is produced by standing-relaxed (SR), and the other corresponds to a metabolic activity of 2 met, which is produced by walking-active (WA) at approximately $3.2\,\mathrm{km\,h^{-1}}$ [61]. The breathing frequency, B_f, and the minute volume, M_v, which is the volume the air exhaled per minute, are enough to describe a transient exhalation flow rate through time. In this work, the values used are those given in [42], as shown in Table 1. From these values, it can be obtained the average time of one exhalation or injection time, $I_t = 60/B_f$, and the volume injected in each exhalation, $V_i = M_v/B_f$. Considering the exhalation as a sinusoidal function [29], it is possible to obtain the exhalation flow rate over time, $\dot{V}$, as follows

$$\dot{V} = \frac{V_i\,\pi}{2\,I_t}\sin\frac{\pi}{I_t}t.$$

The exhalation flow rates of the two modes of breathing along the phases of exhalation are shown in Fig. 3. The artificial lung that reproduces the respiratory function controls the exhaled flow rate as shown in the figure. The exhalation flow emitted through the mouth is expected to develop as a transient jet once it discharges into the environment which is assumed to be at rest with a Reynolds number, Re. The main characteristics of the flows performed for each of the considered exhalation are summarized in Table 1 the maximum Reynolds number, defined as

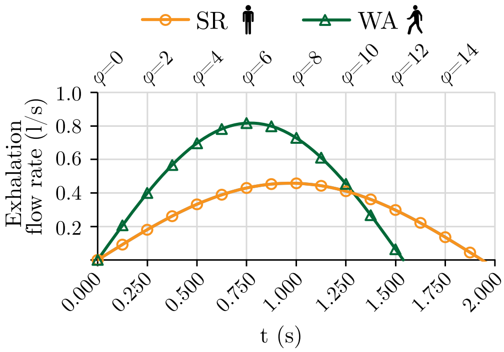

Fig. 3. Respiratory flow rates emitted and phases, φ, recorded for SR and WA exhalations.

Table 1
Characteristics of the two exhalation flows under consideration. Breathing frequency, B_f; minute volume, M_v; maximum velocity in the mouth considering an uniform velocity profile in the mouth determined from its area, a_0, $\hat{u}_0$; Reynolds number, Re; injection time, I_t and volume injected, V_i.

Exhalation	B_f (min^{-1})	M_v (l/min)	$\hat{u}_0$ ($\mathrm{m\,s}^{-1}$)	Re	I_t (s)	V_i (m^3)
SR	15.59	8.92	1.76	2167	1.94	5.65×10^{-4}
WA	20.73	14.38	3.14	3867	1.54	8.01×10^{-4}

Table 2
Experimental parameters used in the SPIV configuration.

Parameter	Value
Laser wavelength	532 nm
PIV Exposure	405 µs
Laser pulse delay	400 µs
Pulse separation time	100 µs
Repetition rate	8 Hz
Stereoscopic imaging configuration	Scheimpflug

$$\mathrm{Re} = \frac{\rho \hat{u}_0 l_0}{\mu},$$

where $\hat{u}_0$ is the average velocity at the mouth in the phase of maximum exhalation, $l_0 = \sqrt{a_0}$ is a characteristic length of the source area, ρ is the air density and μ is the air dynamic viscosity.

2.3. *Stereo particle image velocimetry (SPIV)*

To measure and record three-dimensional vector fields of exhalation velocities in different planes of interest, a SPIV measuring system is used. The layout of the experimental setup and the distances from each plane to the mouth are presented in Fig. 2(c) and (d), respectively.

The system consists of two cameras with CCD sensors, C1 and C2 (FlowSense EO, Dantec Dynamics, Denmark), equipped with optics (AF-S DX NIKKOR 18-105, Nikkon, Japan), that focus the measurement plane illuminated by a light sheet provided by a laser source, L (DualPower 200-15, Dantec Dynamics, Denmark). A synchronizer is used to coordinate image acquisition of both cameras and laser illumination (TimeBOX, Dantec Dynamics, Denmark). The experimental parameters used in the SPIV configuration are summarized in Table 2. To focus correctly on the measurement plane, the cameras are equipped with a high-precision orientation system (Scheimpflug camera mount 9081X0072, Dantec Dynamics, Denmark). To properly illuminate the measurement plane by a laser sheet, the laser light is transmitted via an optical system (Long Light Guide Arm and Base 532 nm, Dantec Dynamics, Denmark). All these elements are mounted on a robotic positioning system (9041T033, Dantec Dynamics, Denmark), identified with T in Fig. 2(c), that let displace the measurement plane to the plane of interest for each trial.

By using the presented setup, measurements were recorded in five transverse vertical planes (P = 1 to P = 5) parallel to the plane in which the outflow orifice through the mouth of the airways model used is located. The five considered planes are situated equally spaced from 10 mm (P = 1) to 50 mm (P = 5) from the mouth orifice along the z axis, considered as the origin of coordinates (see Fig. 2 (d)). Since only one plane can be illuminated in each trial, the experiment must be repeated for each plane and, in order to obtain an average value of the results in each plane, the experiment is performed $N = 50$ trials. Due to the consideration of two types of exhalation, SR and WA, a total of 500 trials have been performed.

A fog generation device (Fog generator: FOG 2010, Safex, Denmark) is used to convey particles generated from an aqueous solution of polyols in the exhalation flow. This is done by introducing the particles into a reservoir from which the artificial lung collects the exhalation air. The particles, with a typical diameter of $1-2$μm, are followed to obtain the velocity field using the SPIV technique. These particles are conveniently mixed in the air supplied to the artificial lung so that the concentration of particles in the flow emitted from the mouth is high enough to get satisfactory results.

The velocimetry system takes a velocity measurement every 0.125 s starting at the instant in which the fog begins to exit from the mouth, considered as instant $t = 0\,\mathrm{s}\,(\varphi = 0)$. Each recorded instant is called a phase, φ. In the two breathing processes considered, the air is exhaled from the mouth during the first 15 phases ($\varphi \leq 15$) in the SR exhalation and in the first 12 phases ($\varphi \leq 12$) in the WA exhalation, with a flow rate function shown in Fig. 3. After that, measurement process continues up to $\varphi = 25$ to record the final part of the air movement in front of the mouth. The different phases considered for each exhalation are indicated in Fig. 3.

The dedicated software used to post-process the pairs of images obtained by the PIV system (DynamicStudio 2015, Dantec Dynamics, Denmark) allows to obtain the velocity field for each individual trial.

This software is set to determine velocity vectors by dividing the images in a series of interrogation areas containing the seeded particles [62,63]. The original 2048×2048 pixels area is divided into interrogation square areas depending on particle seeding density. The interrogation areas are divided into rectangle portions of size 1.471×1.067 mm, and for each one a velocity vector is returned. A cross correlation Gaussian filter and a peak validation procedure are also implemented in order to determine the valid vectors. The invalid ones are rejected and are not considered in the results.

Images are processed through an adaptive multigrid correlation algorithm handling the window distortion and the sub-pixel window displacement. The prediction-correction method is validated for each grid size when the signal to noise ratio of the correlation is above a threshold of 1.1. In average, less than 2 % of the vectors are detected as incorrect. Wrong vectors are corrected by using a bilinear interpolation scheme. The final grid is composed of $32 \times 32\,\mathrm{px}^2$ size interrogation windows with 50 % overlapping leading to a vector spacing of 13.5 px, which represents a spatial resolution of 0.83 mm. In all the cases, the air jet flows were seeded with small oil droplets, 1 to 2 μm in diameter, provided by a liquid seeding generator. When the ratio of particle-image diameter d_{par} to the size of a CCD pixel on the photograph d_{pix} is less than 2, the energy spectrum is overestimated due to the peak locking phenomenon [64]. The present measurement yields 2.5×2.5 px on an average for each particle image. According to [65] the particle images are adequately resolved for the present set of experiments. A systematic inspection of the particle displacement histograms shows a bimodal distribution. This gives sub-pixel accuracy for the determined velocity without peak-locking effects.

In order to balance the in-plane and out-plane errors, an off-axis half-angle of 45° is used. [65] On the other hand, the total error which is an accumulation of the error ratio found in [66] and the bias error ratio is about 1.37 % for the studied angular position of the cameras.

The theoretical analysis of [64] is used to estimate the error on the particle-image displacement. The measurement error for the particle-image displacement would scale proportional to the square of the particle-image diameter, and inversely proportional to the pixel dimension [64]. The error is also inversely proportional to the signal-to-noise ratio. In the present work, the images are obtained with an uncertainty level of 0.05 px and the maximal displacement error is equal to 1 %, 2 %, and 2.5 % for the longitudinal, vertical, and transversal directions, respectively. According to Raffel et al., [67] the rms PIV velocity error is given by

$$\sigma(\epsilon) \approx 0.1[S_{pix} M_S \Delta t]$$

where S_{pix} is the pixel size, M_s is the scale factor of the image, and Δt is the time step between successive images. In the present experiment, $S_{pix} = 24.1$ μm, $M_s = 4$, and $t = 100$ μs. Thus, the rms PIV velocity error is $\sigma(\epsilon) = 0.092\,\mathrm{m\,s^{-1}}$.

In each interrogation area the three components of the velocity vector are obtained

$$\vec{u}_i^k = \vec{u}_i^k\,(x, y, \mathrm{P}, \varphi, Ex)\,,$$

where $i = x, y, z$ denotes the velocity vector component and $k = 1, \ldots, N$ is the index of the trial, being N the number of trials the experiment is repeated. Each measurement is registered as a function of the specific position coordinates of the vector in the measurement plane, (x, y); the measurement plane, $\mathrm{P} = 1, \ldots, 5$; the phase of the exhalation, φ and the type of exhalation, $Ex =$ SR, WA. The coordinate system selected can be seen in Fig. 2(d).

2.4. Average phase method

A time-resolved PIV (TR-PIV) approach is used to analyze the flow behavior, considering the variability of the velocity measurements obtained in each repetition, k, of the same experiment. [67]. This technique is based on repeating the experiment enough times to allow, on the one hand, to capture the physics common to the experiment, and on the other hand, to analyze the variability of the results [68]. As already indicated, for each experiment, SR and WA exhalations, a total of $N = 50$ trials are performed.

As already mentioned, to capture the unsteady structure of the flow for each one of the 50 exhalations, 25 equally time-spaced SPIV measurements (0.125 s) are performed, obtaining a three-dimensional velocity vector field in each measurement $\vec{u}^k = (u_x^k, u_y^k, u_z^k)$. To ensemble all these velocity fields, an average phase method (APM) has been implemented as it has been previously done for the study of similar flows [58,60,69,70] and the same experimental technique [71].

For a given plane and phase, the average value of each component of the velocity is calculated in each point of the plane from the measurements obtained in all the trials as follows,

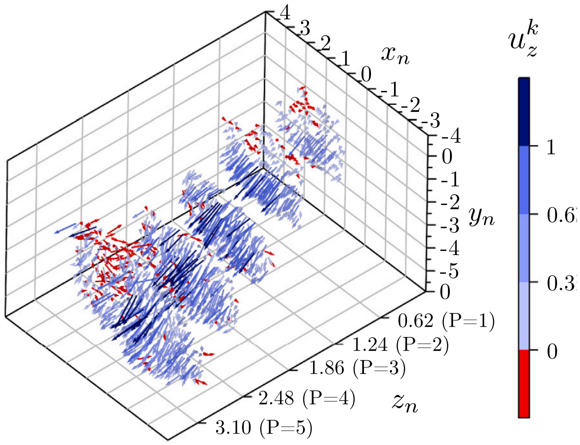

Fig. 4. Individual measurements for the five planes of interest showing the velocity vector $\vec{u}^k$. The vectors are colored considering their z-component, u_z^k. Only one from each nine vectors captured are shown in the figure and the z-dimension has been magnified by a factor of 3.25 for a better visualization of the data.

$$U_i = \frac{1}{N}\sum_{k=1}^{N} u_i^k.$$

The turbulence intensity, u'/U, is used as a measure of dispersion of the results [58], being $u' = \sqrt{\frac{1}{N}\sum_k^N \left(U - u^k\right)}$ the value of the root mean square value of the velocity fluctuations, U and u^k the module of the average velocity and the instantaneous velocity, obtained at each point, respectively.

The center of the jet is considered to be located at the point of maximum velocity for each plane and phase,

$$\hat{U}_{cl}(\mathrm{P},\varphi) = \max_{(x,y)\in P} U(x,y,\mathrm{P},\varphi),$$

being the jet centerline the line that joins these points. The perimeter of the jet section are considered to be located where the value of the velocity modulus is reduced to 5 % of its maximum value at the centerline, $\hat{U}_{cl}$.

To facilitate comparison of the results obtained in this study, distances and velocities are normalized by using the area of the mouth and the maximum averaged velocity registered for each experiment, $\hat{U}_{Ex}$, as shown in Eq. (1) and Eq. (2), respectively,

$$x_n = x/\sqrt{a_0};\ y_n = y/\sqrt{a_0};\ z_n = z/\sqrt{a_0}, \tag{1}$$

$$U_n = U/\hat{U}_{Ex}, \tag{2}$$

where,

$$\hat{U}_{Ex} = \max_{\mathrm{P},\varphi} \hat{U}_{cl}(\mathrm{P},\varphi). \tag{3}$$

Therefore, to obtain the normalized velocity values, first of all the experimental values recorded through the trials carried out are averaged and then normalized using $\hat{U}_{Ex}$.

3. Results

3.1. Description of the flow. Individual trials

Fig. 4 shows a typical instantaneous velocity field, $\vec{u}^k$, corresponding to the measurements obtained in one of the repetitions, k, of the experiment for the SR exhalation at different planes. These vectors correspond to the phase $\varphi = 8$, in which the flow rate through the mouth is maximum. This snapshot view allows to have an idea of the flow evolution of the flow in the proximity of the mouth. In Fig. 4, the obtained vectors are colored considering the magnitude of the vector component in the z direction, u_z^k. Vectors with a negative u_z^k component are shown in red while those with a positive u_z^k component are shown in blue, with an intensity proportional to the magnitude of this vector component. The results show that the maximum velocity values are recorded in the jet core for all planes. The velocity modulus decreases radially. It can be checked that the maximum velocities are not obtained in the P = 1 plane, but in planes further away from the nozzle. In the jet boundary zone, which is the limit perimeter of the jet's area of influence, at the periphery of the jet, a number of vectors with negative u_z velocity are observed in all planes. These counter flowing vectors are clustered in specific areas of the periphery and their grouping can respond to the formation of vortices in the plane. The direction of the vectors shows a different behavior in the velocity field displayed for each distance from the mouth. While the planes closer to the mouth show more ordered vector patterns, when moving away, the vectors show different individual patterns.

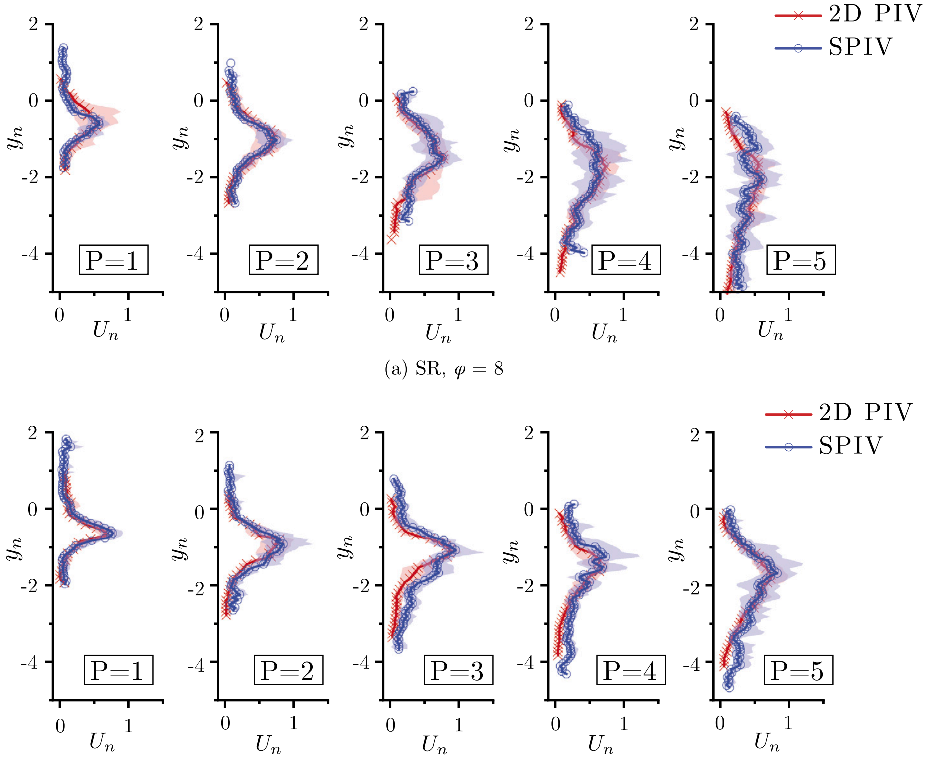

(a) SR, $\varphi = 8$

(b) WA, $\varphi = 6$

Fig. 5. Comparison between velocities recorded with 2D PIV and SPIV techniques. The variations of the individual measurements are shown in the image in the form of an error band with a lighter color.

Table 3
Maximum velocities obtained for each exhalation, $\hat{U}_{Ex}$, and normalized distance to the mouth, $z_n(\hat{U}_{Ex})$, and phase where they have been registered, $\varphi(\hat{U}_{Ex})$. Comparison between 2D PIV and SPIV techniques.

	SPIV			2D PIV [60]		
	$\hat{U}_{Ex}$	$z_n(\hat{U}_{Ex})$	$\varphi(\hat{U}_{Ex})$	$\hat{U}_{Ex}$	$z_n(\hat{U}_{Ex})$	$\varphi(\hat{U}_{Ex})$
SR	$2.34\,\mathrm{m\,s^{-1}}$	1.86	11	$2.06\,\mathrm{m\,s^{-1}}$	1.93	11
WA	$3.10\,\mathrm{m\,s^{-1}}$	1.86	7	$2.71\,\mathrm{m\,s^{-1}}$	2.29	7

3.2. Validation of the measurement technique

The results obtained using the SPIV technique are compared with those obtained using the 2D PIV technique for the same scenario and environmental conditions in order to validate the experimental technique by using contrasted data published in [60]. Fig. 5 shows a comparison of the results for U_n obtained with both techniques and the APM methodology in the vertical section at $x = 0$ in the planes $\mathrm{P} = 1, \ldots, 5$, and the phases of maximum flow emission through the mouth for each exhalation: $\varphi = 8$ for SR $\varphi = 6$ for WA. From Fig. 5, which represents the comparison for SR breath, Fig. 5(a), and WA breath at Fig. 5(b), it is possible to observe that there is a good agreement between the measurements recorded with both techniques. The difference between the maximum velocity recorded in all the cases shown remains below $10\,\%$ in all the planes and phases considered.

Regarding the dispersion of the results, it can be verified that it is high for both measurement techniques, which justifies the use of the APM methodology to analyze the physics of the flow. Nevertheless, a study of the convergence of the results through the trials has been carried out and shows that the number of trials is sufficient, it can be seen in Appendix B. The maximum absolute error is obtained at the points of maximum velocity registered, in the central part of the jet. In this area, the maximum values of results standard deviation are also found, with values around 0.4.

It must be taken into account that the results obtained with the different techniques shown in Fig. 5 have been normalized with their respective maximum velocities, $\hat{U}_{Ex}$, obtained with Eq. (3), from the maximum velocity registered for each plane and phase, $\hat{U}_{cl}$. The maximum velocity, $\hat{U}_{Ex}$, the normalized distance to the mouth, $z_n(\hat{U}_{Ex})$, and the phase, where this occurs $\varphi(\hat{U}_{Ex})$, obtained with both techniques are shown in Table 3. These results show that the maximum velocity values recorded for the two types of

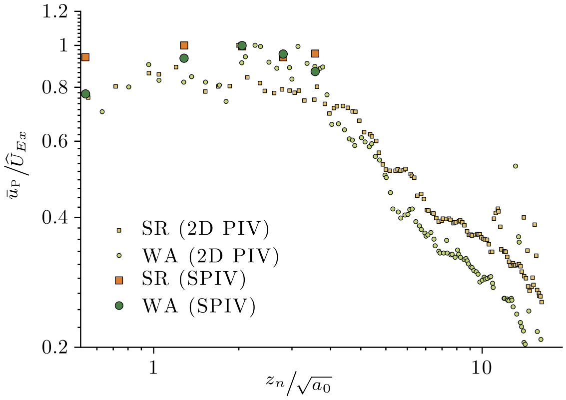

Fig. 6. Decay of jet velocity with distance from the mouth. Comparison between velocities obtained with 2D PIV and SPIV techniques.

exhalation are similar for the two measurement techniques employed. However, a higher velocity is observed in the case of the measurements taken using the SPIV technique, which may be due to the fact that this technique records the three components of the velocity whereas the 2D PIV technique only records the velocity components in the longitudinal yz-plane, and it is possible that the x-component of the velocity increases its modulus with the distance to the mouth. Besides, it is also possible that the maximum velocity is reached outside of the longitudinal plane.

Another aspect that has been compared is the velocity decay with the distance to the mouth that has been assessed using $\bar{u}_{\mathrm{P}}$, which is the mean of the peak values obtained in each plane in the different trials, regardless of the phase in which it occurs. Note that it is not a value obtained using APM.

The comparison shown in the Fig. 5 shows consistent results between the two measurement techniques used, so that the use of the results obtained through the SPIV technique allows to increase the knowledge about the mechanisms of jet development formation obtained from the analysis of the two-dimensional measurements. Fig. 6 shows the comparison of the results obtained for the velocity decay with SPIV and those obtained using the 2D PIV technique [60] for the same experimental situation.

Overlaying the results obtained for this study using the SPIV technique with those obtained with the 2D PIV study [60], it can be noted that the agreement between them is good. In this comparison it must be taken into account that the results obtained with the different techniques have been normalized with their respective maximum velocities shown in Table 3. The measurement planes of the SPIV are located in the developing region of the jet before its transition to the characteristic decay region [72]. In this zone it can be seen a slight increase in the value of $\bar{u}_{\mathrm{P}}$, that is more significant in the case of WA exhalation. This is observed in the results obtained with both techniques.

The velocity $\bar{u}_{\mathrm{P}}$ increases with the distance to the mouth up to reach a maximum at a distance in the range of $2l_0$, for all cases. In the case of the SPIV study there are only five discrete measurements in the preferred direction of the flow, whereas the records in the case of the 2D PIV study are continuous. This acceleration of the flow outside of the mouth that may be associated to the vena contracta effect, has been observed by other authors in experimental studies of exhalations, as, for example, Vansciver et al. [28] in experiments with coughs, and in experimental studies of free jets when using nozzles with a sharp shape [73]. The phases in which the maximum velocities are recorded are the same regardless of the measurement technique used. In both cases the maximum velocities are recorded after the phase of maximum flow emission through the mouth, which is due to the propagation time required for the emitted flow to reach the point of maximum velocity.

3.3. Maximum exhalation velocity progression

Fig. 7 shows the time evolution of the maximum velocity modulus $\widehat{U}$, obtained using the APM methodology, for the different planes and the two types of breathings, SR at Fig. 7(a) and WA at Fig. 7(b), together with the reference velocity modulus expected in the mouth ($z = 0$) considering the transient flow rate throughout the exhalations and its opening area, a_0. It is observed that the progress of $\widehat{U}$ throughout the phases shows a sinusoidal trend, which is broken in the final part of the exhalation with a smoother decrease of the peak velocities in the final phases. This behavior is reasonable given that the function that models the time evolution of the flow rate emitted through the mouth has a sinusoidal shape, following the results obtained by other authors, such as Zhang and Johari [74], that study the effects of acceleration on the injection velocity turbulent jets and observed that for each acceleration pattern, the temporal evolution of the front position had the same functional form as the velocity. The maximum velocity evolution is similar for all planes, especially in the initial phases of exhalation, with similar velocity values in all planes. Once the maximum velocity is reached, the final phases of exhalation show a different trend, especially in the case of WA breathing, (Fig. 7(b)). This lack of symmetry in the final part of the velocity evolution is compatible with the puff-like behavior of the exhalation, maintaining a more irregular final velocity distribution [75].

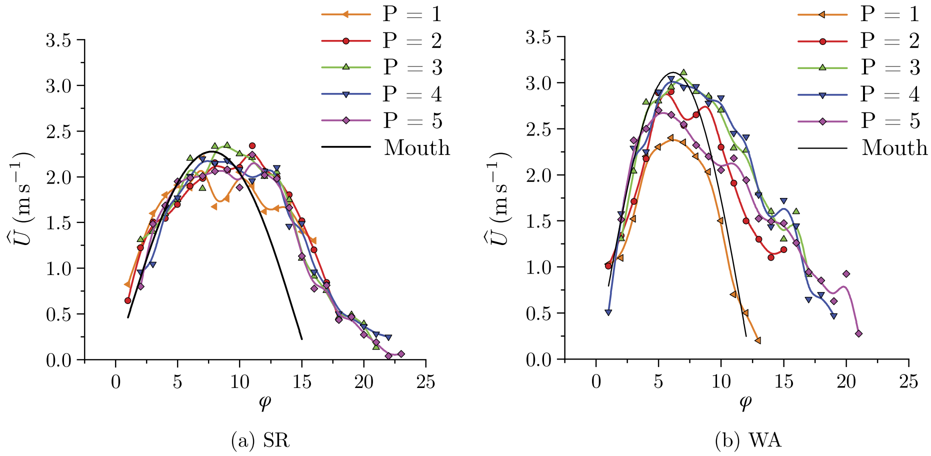

Fig. 7. Time evolution of the maximum velocity modulus, $\widehat{U}$, obtained in each plane and phase throughout the two exhalations considered. The expected velocity at the mouth, determined from its area, a_0, is also shown.

3.4. Influence zone of each exhalation

The influence zone of each plane is the cross-sectional area in which valid velocity records are obtained for each phase. Outside this area, the presence of particles is not appreciable, so no valid velocity values are obtained. In order to facilitate the visualization of valid results, this area is left empty in the final representation. Particle seeding is carried out in the air from which the artificial lung is fed, so the fluid in the exhalation contains a high concentration of particles, which is reduced in the contour of the jet due to entrainment effects. Taking this into account, it may be considered that the influence zone corresponds approximately with the cross-section of the jet. The results of the normalized velocity modulus, U_n, for the plane $\mathrm{P} = 3$ are shown as contour plots for a selection of representative phases in Figs. 8(a) and (b) for the SR and WA exhalations, respectively. The area of influence of each contour line plot, a_φ, is expressed as a function of the cross sectional area of the mouth a_0. In Fig. 8 it is possible to observe that the area of the influence zone increases significantly from the beginning of the exhalation up to a maximum value is reached, and then it reduces its area progressively until some phases after the end of flow emission. When comparing the time evolution of the areas of influence of the two exhalations, it is possible to identify that there is a quicker increase in the area of influence in the case of the WA exhalation and that the maximum area of influence obtained is larger than in the case of SR. It is interesting to notice how the delay of the phase in which the maximum of the area of influence is reached ($\varphi = 12$ and $\varphi = 10$ in WA and SR exhalation, respectively) with respect to the phase of the maximum flow emission through the mouth ($\varphi = 6$ and $\varphi = 8$, respectively) is significantly higher. This fact may be due to a higher entrainment of the surrounding air. These results are directly related to the higher peak flow velocity recorded for WA and to the longer injection time obtained in SR. It has been experimentally proven that exhalations performed at a higher metabolic rate have a relative longer duration of time [42].

As the area of the cross section increases, the initial approximately circular shape of the jet section becomes an oval shape, up to a maximum spreading. Eventually, as the area decreases, the shape of the cross section of the jet recovers its circular shape. There are few experimental studies that analyze the cross-section of the flow in the exhalation, as the work of Thacher et al. [25], that observed a non-circular cross section of the flow through hot-wire measurements. This lack of axisymmetric velocity distribution may be related to the internal geometry of the airways which influences the velocity field at the jet discharge and affects the experimental data obtained. In addition, it must be taken into account that the measurement planes used in this work are vertical and the exhalation flow jet, as will be shown later, has a certain downward deviation, so that the vertical dimension of the influence area would be higher in the vertical plane if the velocity distribution was axisymmetric. Non-axisymmetric distribution of the velocity has been identified in a few experimental studies of respiratory phenomena such as cough [25] and speaking [59]. The lack of axisysimetry can be due to the shape of the nozzle, it is known that an oval shape of the opening through which the air is emitted affects the vortices generated avoiding axisymmetry, as presented in the results. This has been verified in both numerical [76] and experimental studies [60,77].

The results of the normalized velocity modulus, U_n, recorded for the phase of maximum emitted flow for each type of exhalation, are shown as contour plots in Fig. 9(a) for SR exhalation and in Fig. 9(b) for WA exhalation. This figure shows the results obtained for each of the planes of interest ($\mathrm{P} = 1, 2, \ldots, 5$), located at different distances from the mouth and allows to analyze the flow behavior with the distance from mouth. The area of influence of each contour line plot, a_φ, is expressed as a function of the area of the mouth a_0. In Fig. 9, it is observed that the area of influence of the jet increases with the distance from the mouth. This is the usual behavior of a jet, which increases its area of influence due to the entrainment of the surrounding air [72]. It is possible to identify that the cross-sectional area of influence is shifted towards negative values of y_n with distance. This situation has been previously observed in many 2D PIV studies [28,54,60] and visualization techniques [45,47]. In addition, a horizontal shift towards areas of negative x_n directly proportional to the distance from the plane to the mouth is observed. This phenomenon, that occurs in both exhalations

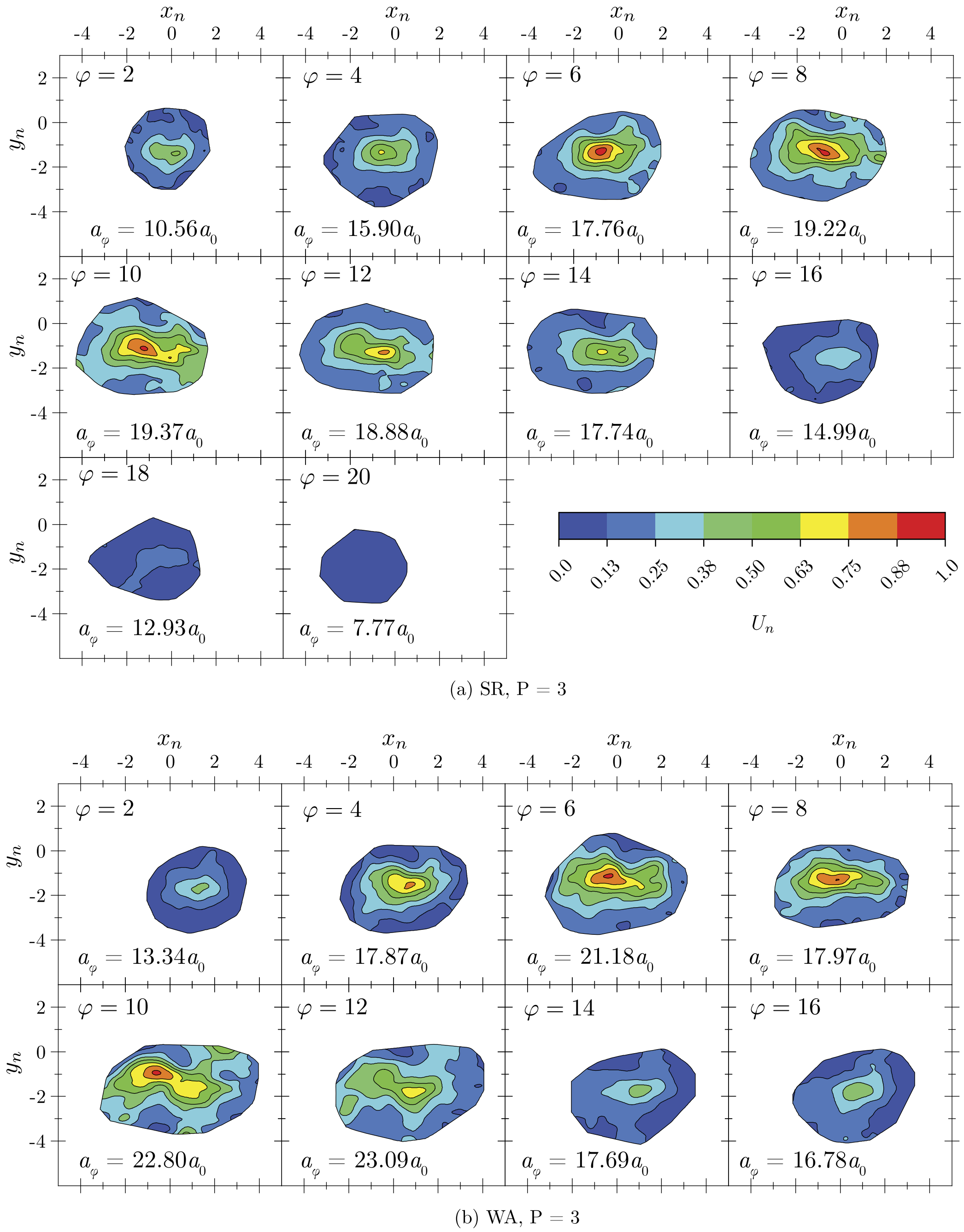

Fig. 8. Time evolution of the velocity modulus, U_n, in the plane P = 3, for the two exhalations studied.

considered, has been scarcely reported in the literature, among other reasons because there are few results of the velocity distribution in transverse sections. This deviation can be observed in the results presented by Xu et al. [47] and Han et al. [53], although it has not been highlighted by the authors.

The maximum velocity is recorded in the P = 3 plane for both experiments. The fact that the maximum velocity is not recorded in P = 1, the plane closest to the mouth, can be explained by the vena contracta effect as it has been previously described in Section 3.2.

The vorticity in the z-direction of the flow, ω, in the P = 3 plane at the instant of maximum exhalation flow has been obtained for the two exhalations studied, Fig. 10. It can be observed how the external flow entrainment process that generates the mixing inside the jet presents Kelvin-Helmholtz type structures for SR, Fig. 10(a), and for WA, Fig. 10(b), exhalations. This fact has been previously observed in other studies of transient jets using the same technique and experimental setup used in this study [78].

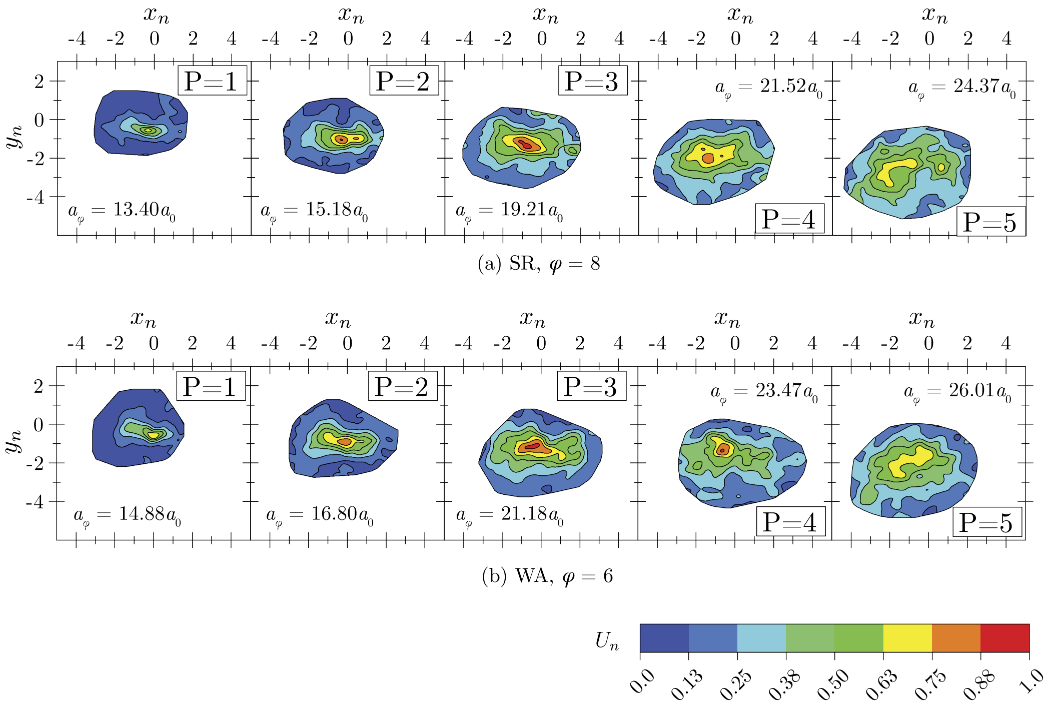

Fig. 9. Distribution of the velocity modulus, U_n, in the different measurement planes for (a) $\varphi = 8$, SR exhalation, and (b) $\varphi = 6$, WA exhalation.

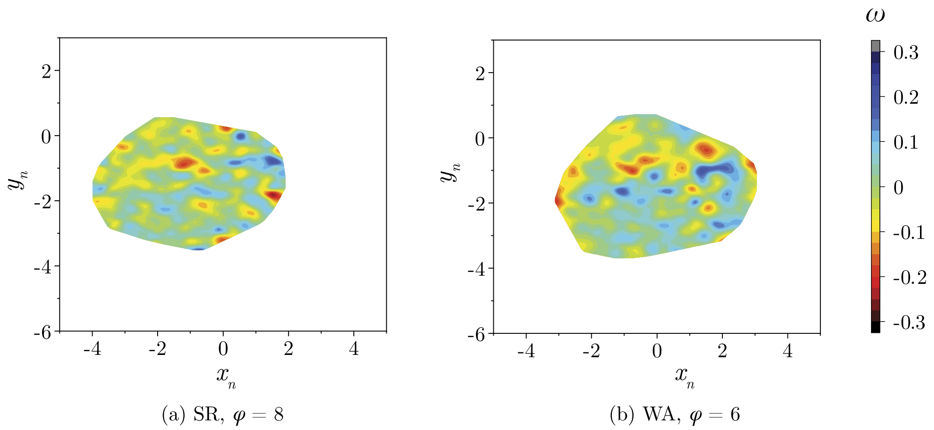

Fig. 10. Vorticity, ω, in P = 3 for the maximum exhalation flow phases (a) $\varphi = 8$, SR exhalation, and (b) $\varphi = 6$, WA exhalation.

3.5. Variability of the results in the boundary of the transient jet

To analyze the variability of the results obtained, the turbulence intensity, defined as u'/U, is used. Fig. 11 shows the time evolution of u'/U along the different phases of each of the two exhalations considered for the P = 3 plane. Fig. 12 shows the spatial evolution of the velocity results for the maximum emitted flow rate phases of each exhalation. The u'/U distribution shown in Fig. 11 is quite irregular, although it can be observed an internal zone where this value is much lower for both exhalations studied, SR, Fig. 11 (a) and WA, Fig. 11 (b). The proportion of the section occupied by this internal area is higher in the case of SR exhalation, Fig. 11 (a). The value if u'/U is, in general, higher near the boundary which is consistent with a high turbulent activity in the mixing layer. In the vicinity of the boundary of the area of influence, small areas with high values of u'/U appear corresponding with areas where the average velocity is low and there is also a certain variability in the measurement, possibly due to a lack of concentration of particles.

The observation of the results presented in Fig. 12 allows us to analyze the spatial development of u'/U along the jet for SR, Fig. 12(a), and WA, Fig. 12(b), exhalations.

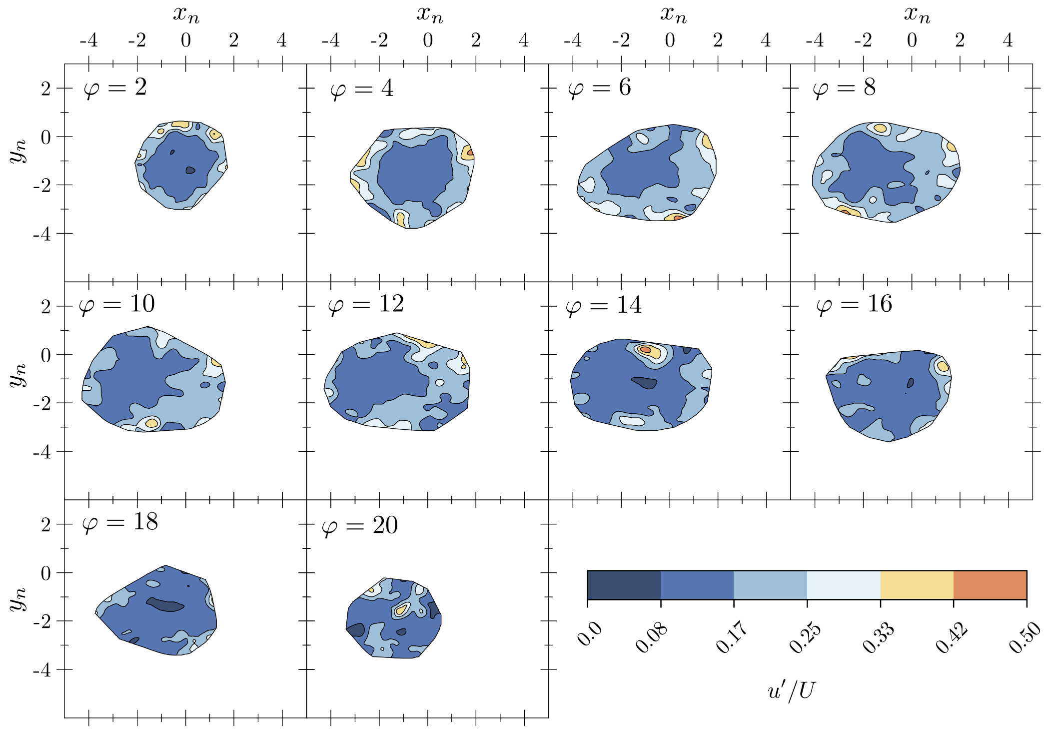

(a) SR, P = 3

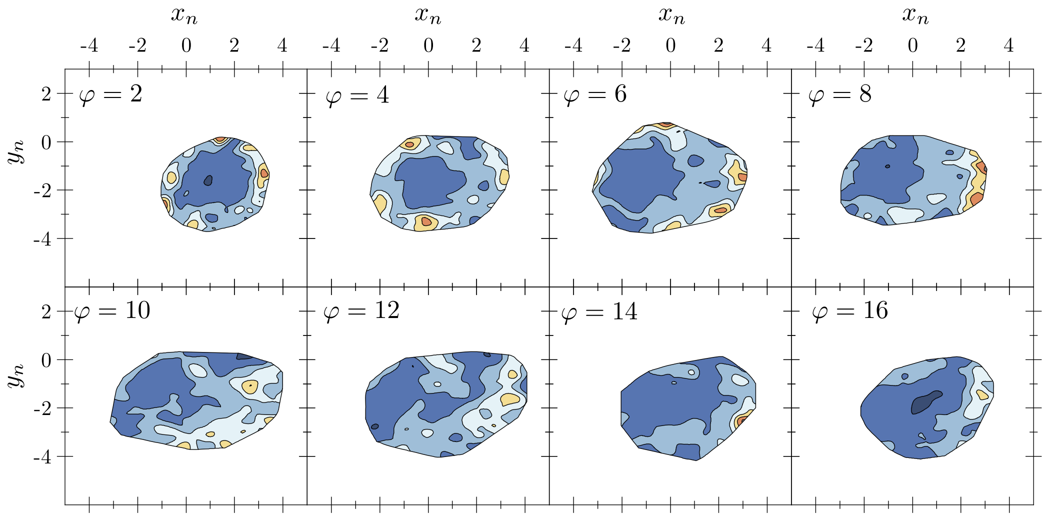

(b) WA, P = 3

Fig. 11. Time evolution of the distribution of u'/U in plane P = 3 throughout phases for the two exhalations considered.

In the center of the zone of influence of the jet, a zone of low u'/U is identified in all planes, coincident with the zones where the velocity modulus is maximum. This zone can be identified with the jet core. At the periphery of the jet cross section, an increased u'/U in all planes is identified. The central low u'/U zone decreases in size with distance from the mouth, implying an increase in the mixing zone with the ambient fluid.

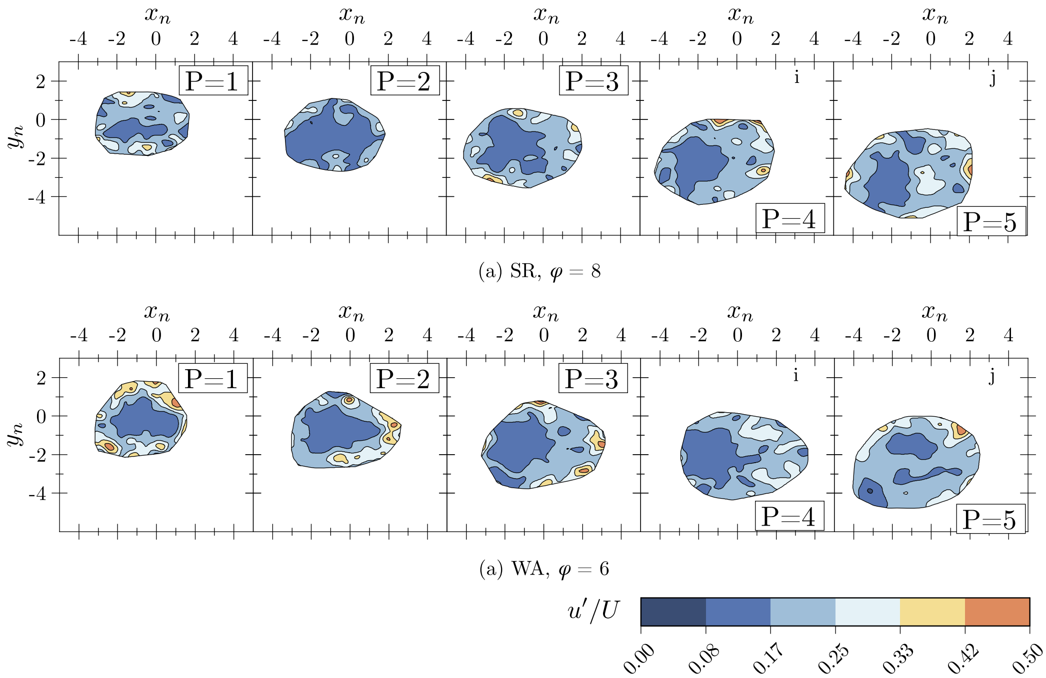

Fig. 12. Registers of u'/U for the maximum exhalation phase for the planes of interest.

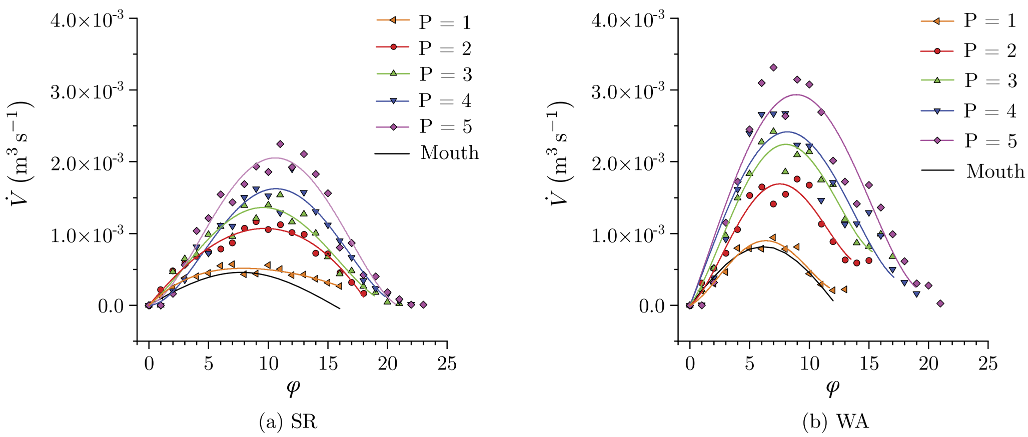

Fig. 13. Flow rate, $\dot{V}$, obtained for each of the exhalations considered in the different planes studied.

3.6. Flow rate and entrainment

The flow rate $\dot{V}$ through each plane is obtained from the velocity profiles as,

$$\dot{V} = \int_S \vec{U} \cdot \vec{n}\, \mathrm{d}S,$$

where S is the cross-sectional area of the jet for the plane and $\vec{n}$ the unit vector normal to S.

Considering the velocity fields obtained for the different phases in each experiment, the flow rate through each plane, $\dot{V}$, is obtained. Results are shown in Fig. 13 along with a polynomial fit to the data collected for each plane P. For each phase, exhalations show an increase in volumetric flow, $\dot{V}$, with increasing distance from the mouth. While in the P = 1 plane the flow is almost similar to that emitted through the mouth, the following planes show a considerable flow rate increment for the same phase what indicates a higher flow entrainment. This increment is higher in the planes furthest from the mouth. The increase in $\dot{V}$ with jet advance is due to air entrainment caused by the presence of turbulent structures at the jet periphery, that have already been identified in Fig. 11.

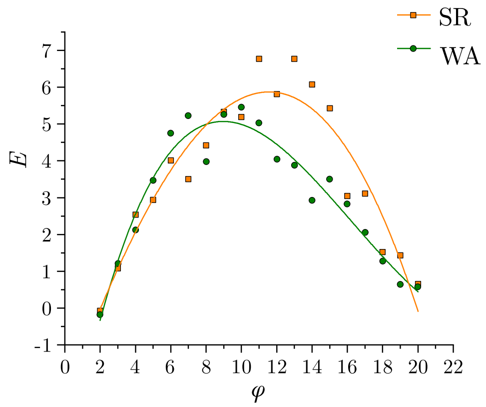

Fig. 14. Flow entrainment, E, for each type of exhalation through φ.

This flow entrainment is higher in the case of WA exhalation, Fig. 13(b), due to the higher exhalation flow rate emission which is consistent with the hypothesis widely accepted that the entrainment velocity in a jet is proportional to the velocity of the flow (see, e.g., [12]). Once the emitted flow reaches its maximum and starts to decrease, so does the flow that passes through the planes under study, although, the decrease shows a delay with respect to that emitted through the mouth for both exhalations SR, Fig. 13(a), and WA, Fig. 13(b). For each plane, the points of maximum $\dot{V}$ are reached at later phases as the distance to the mouth of the plane considered increases. The flow delay is similar in both exhalations and approaches 0.5 s (i.e., equivalent duration of four phases) in the final phases of each exhalation. The dependence of the ambient air entrainment on the injected flow rate has previously been studied in transient jets (see, e.g., [79,80]).

The flow entrainment, E, along the time course of the exhalation is obtained by considering the difference between the flow rate in the last plane, $\dot{V}(\mathrm{P}=5,\varphi)$ and the flow rate emitted through the mouth for the same phase, φ, $\dot{V}(\mathrm{P}=0,\varphi)$, normalized with the average emitted flow rate $\bar{\dot{V}}$,

$$E(\varphi)=\frac{\dot{V}(\mathrm{P}=5,\varphi)-\dot{V}(\mathrm{P}=0,\varphi)}{\bar{\dot{V}}}.$$

The entrainment results obtained for the two types of exhalations considered are shown in Fig. 14 together with a polynomial fit to the data collected for each exhalation.

From the data presented in Fig. 14 it can be seen that the entrainment increases with the emitted flow with a similar rate in both types of exhalation. The maximum value of entrainment for both types of exhalation occurs with a certain delay with respect to the time at which the emitted flow rate reaches the maximum. In the case of the SR exhalation this delay is greater so that the entrainment relative to the average flow rate emitted is also greater. Once the entrainment begins to decrease, it can be seen how the rate of decreasing is higher in the SR case. Considering the type of exhalation WA and taking into account the time of emission, the duration of the airflow is relatively longer in the case of this exhalation.

3.7. Opening angles of the jet and centerline

To determine the jet opening, the velocity modulus is used as a reference. As previously mentioned, the jet boundary is considered to be found when the value of the velocity modulus is reduced to 5 % of its maximum value at the centerline, $\hat{U}$. This criterion to determine the width of the jet has been followed by [58,60,70], although other authors have used different values, e.g. 1 % in Han et al. [53], or 50 % in VanSciver et al. [28]. From the velocity modulus data obtained for each of the planes and phases, the horizontal and vertical aperture of the jet is delimited for each phase, determining the extreme points of the velocity field that meet the above condition at the different planes. Knowing the extents of the jet in each phase and plane of interest, it is possible to determine the time evolution of the jet limits by means of the linear fit to the extreme points obtained in the five measurement planes. Two different opening angles are defined: the horizontal aperture in the xz-plane, α_o, and the vertical aperture in the yz-plane, θ_o. On the other hand, considering the point where maximum velocity is registered for each plane, $U/\hat{U}=1$, it is possible to determine the centerline direction in each phase by linear regression and the angles that forms with the vertical (yz) and horizontal (xz) planes, θ_{cv} and θ_{ch}, respectively. In Fig. 15 an example of the mentioned angles is shown. While Fig. 15(a) shows the velocity modulus obtained for the different planes considered in perspective, Figs. 15(b) and (c) show the projection in the yz and xz planes respectively.

Fig. 16(a) shows the angles θ_{ch} and θ_o obtained in the vertical yz-plane for both SR and WA exhalation, while Fig. 16 (b) shows the angles α_{ch} and α_o obtained in the horizontal xz-plane. Only values with a coefficient of determination in the linear fit higher than 95 % are displayed in these figures.

It is observed that a good regression fit has not been obtained for the periods comprising the initial and final parts of the exhalations, especially in the angles corresponding to the horizontal plane. This lack of homogeneity of the results may be due to the initial formation of ring-shaped vortex structures [81] and the absence of flow influence in the planes farthest from the mouth in

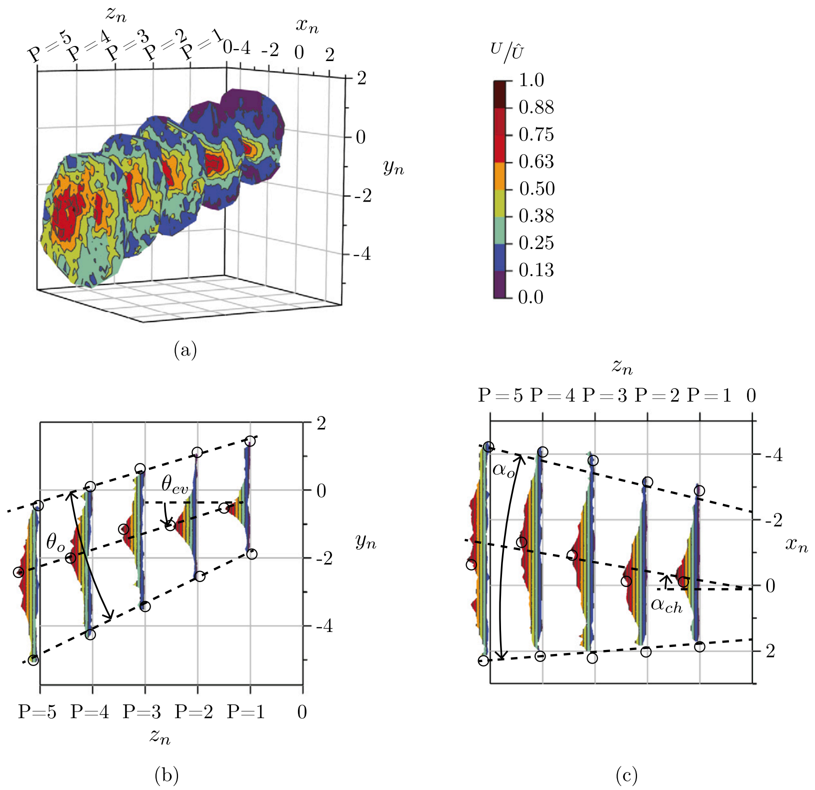

Fig. 15. Jet opening angles definition. (a) Measurements of the velocity modulus obtained for the different planes considered, (b) projection onto the $yz-$ plane and (c) projection onto the $xz-$ plane.

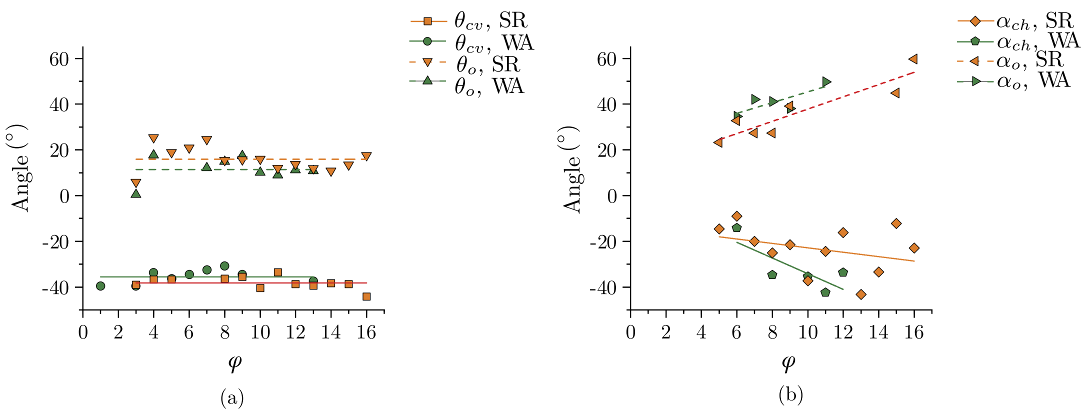

Fig. 16. Opening and centerline deviation of the jet along the different phases for both SR and WA exhalation. (a) Angles obtained in the yz-plane and (b) angles obtained in the xz-plane.

the first phases of the exhalation. In the final part of the exhalation, due to the process of deceleration, there is not a clear definition of the direction and opening of the flow. Similar phenomena has been observed in other respiratory events [82]. For the considered data, it is observed that the results obtained are very similar for the two exhalations for exhalation openings and centerlines. The behavior of the centerline in the vertical plane, θ_{cv}, is similar for the two modes of breathing, forming an angle between -35° and -40°, as it can be seen in Fig. 16(a). The angle does not change throughout the exhalation. Results obtained for vertical opening jet angles are very similar to the ones obtained for research on real subjects, $(30.3^\circ(3.8^\circ{-}3.3^\circ))$ in [29] and $(36^\circ(\pm 6^\circ))$ in [47], but they are higher to those obtained when an oversimplification of the airways is used [58]. Different numerical studies have addressed the study of human exhalation flow. Previous studies such as Villafruela et al.[83] or Gao and Niu [84] show vertical deviations of the flow. However, the emission of the breathing flow at a different temperature than in this study makes direct comparison of the results not viable.

The value of the centerline deviation in the horizontal plane, α_{ch}, tends to increase, becoming more negative as the phases of exhalation progress. For the initial phases of exhalation it shows a value close to -10° and a gradual increment to values close to -35°. It can be identified that the flow deviates significantly over the course of the exhalation. This deviation may be due to asymmetries in the geometry of the airways analyzed. Exhalation horizontal jet opening angles cannot be compared with previous research because of the lack of investigation in the topic. Nevertheless, for other types of respiratory phenomena, such as in the study of coughing, similar angles are identified as, for example ($-13^{\circ}/-15^{\circ}$) in [53].

Analyzing the results obtained for the vertical opening angle θ_o, it is observed that, starting from low opening angles, between 0° and 5° in the first phases of exhalation it deviates towards higher values in the phases of emission of the maximum exhalation flow through the mouth for each breathing mode $\varphi = 6$ and $\varphi = 8$. From these phases, the value of θ_o tends to reduce and stabilize around 15° as the phases progress for both WA and SR. Analyzing the results obtained for the horizontal opening angle α_o, it is observed that its value increases steadily throughout the exhalation. It starts from values around the initial 25° for $\varphi = 5$ and reaches registers close to 60° once the flow stops emitting through the mouth. This may be associated to the widening of the cross section in the horizontal direction.

4. Conclusions

An experimental study of the breathing exhalation flow for two different metabolic rates using Resolved Stereo PIV in transverse planes located in the vicinity of the mouth has been carried out. This study has allowed us to obtain three-dimensional velocimetry results for the spatial and temporal evolution of the flow in the developing jet region. The following conclusions can be drawn from the results obtained:

- A validation of the results has been carried out by comparing them with those obtained in previous works using a 2D PIV technique. The average velocity profiles corresponding to the longitudinal plane and the velocity decay rate have been satisfactorily compared.
- It has been shown that the velocity distributions measured in the cross sections of the exhalation jet are far more complex than those that obtained with simplified airway models or those corresponding to jets emitted from nozzles. The non-axisymmetric distributions obtained vary with time and tend to adopt an oval shape even when the shape of the mouth is round.
- Time evolution throughout the exhalation of the shape of the area of influence of the jet in the different transverse planes has been studied. It has been identified that, starting from an approximately circular shape corresponding to that of the mouth, the area of influence of the jet adopts an oval shape during the first phases of exhalation, possibly influenced by the internal shape of the airways. However, when the flow emission through the mouth stops, in the final part of the phases considered the area of influence of the jet becomes circular again. The flow changes from jet to puff-like behavior as the flow emission ceases. This time evolution has been observed in the different measurement planes.
- It has been found that the temporal variation of the maximum velocity in each of the planes follows a similar trend to the sine function used to represent the emitted exhalation flow, although in the final phases the attenuation of the velocity is slower due to a residual air flow that remains for a certain time after the end of the flow emission in the mouth. It has been seen that the maximum flow velocity is not reached at the exit of the mouth, but is reached at a certain distance downstream from the mouth, due to the effect of the vena contracta. This phenomenon is also observed in simplified airway models.
- The volumetric flow rate has been calculated in each of the measurement planes, which has made it possible to quantify the entrainment flow rate. Its temporal evolution has been studied and it has been found that it increases proportionally to the flow velocity and that it decreases when the flow emitted in the exhalation decreases, with a delay that depends on the type of exhalation. It has been also found that, while in the WA case a higher entrainment in absolute value is reached, the entrainment referred to the mean emitted flow is higher in the case of the SR exhalation.
- The temporal evolution of the jet centerline direction and the jet opening angles in the vertical and horizontal planes have been analyzed. It has been found that while in the horizontal plane the time variation of the flow direction and the opening angle is small, in the vertical plane there is a significant variation of the opening angle, which is compatible with the evolution of the shape of the section which, as we have seen, widens in the horizontal direction. On the other hand, a deviation of the jet in the horizontal direction away from the plane of symmetry has been observed, which is possibly due to a lack of symmetry in the airways of the realistic model used.

This work has allowed to increase the knowledge of the flow in breathing, which, is a potential source of pathogen transmission. Despite the fact that a greater number of tests would have been desirable to achieve a smoother mean velocity distributions in each exhalation, the results obtained have made it possible to analyze the main characteristics of expiratory flow in the vicinity of the mouth, especially regarding to the temporal evolution of the velocity distribution in cross sections, where, to the authors' knowledge, there are no previous experimental results.

Table A.1
Morphometry of the trachea-bronchi region. The table collects three geometrical variables to describe the different levels of divergence, the diameter of the conduits, the angle of branching and the length of each conduit. Each variable is described through its mean value, the range between the maximum and minimum value found and the standard deviation of the data.

Generation level	No. of branches	Diameter (mm)			Angle of branching (°)			Length (mm)		
		Mean	S.d	Range	Mean	S.d	Range	Mean	S.d	Range
0	1	20.5	-	-	0	-	-	110.9	-	-
1	2	16.9	2.8	14.3-18.9	30.5	10.0	23.5-37.6	43.7	19.9	29.6-57.8
2	4	11.4	3.2	8.4-15.4	30.7	11.7	21.2-47.4	14.3	6.3	7.0-22.4
3	8	6.7	1.8	2.7-8.4	25.8	12.2	7.4-43.0	11.5	7.0	2.7-20.7
4	16	5.3	1.3	2.2-7.2	22.9	12.9	1.2-45.0	12.4	4.8	3.1-24.2
5	32	3.7	1.1	2.1-7.5	15.9	7.2	5.5-40.1	14.4	9.8	4.2-49.6
6	52	3.2	0.8	1.7-5.6	22.6	19.0	0.0-86.4	13.2	10.0	0.7-42.4

Limitations of the study

The exhalation flows used respond to a simplified model already referenced in the article, which takes into account the characteristics of the person and the metabolic activity carried out, it is not a real breathing of a person. The airway model used is rigid, so the airway walls do not change their position during exhalation; this is not the case for human airways, so the exhaled flow may be somewhat different.

CRediT authorship contribution statement

F.A. Berlanga: Conceptualization, Data curation, Formal analysis, Investigation, Methodology, Resources, Software, Supervision, Validation, Visualization, Writing – original draft, Writing – review & editing. **P. Gomez:** Investigation, Resources, Supervision, Validation, Writing – original draft, Writing – review & editing. **A. Esteban:** Investigation, Resources, Software, Validation, Visualization, Writing – original draft, Writing – review & editing. **L. Liu:** Conceptualization, Data curation, Formal analysis, Funding acquisition, Investigation, Methodology, Project administration, Resources, Supervision. **P.V. Nielsen:** Conceptualization, Data curation, Formal analysis, Funding acquisition, Investigation, Methodology, Resources, Supervision, Validation.

Declaration of competing interest

The authors declare that they have no known competing financial interests or personal relationships that could have appeared to influence the work reported in this paper.

Appendix A. Detailed information on the respiratory system model

This section intends to provide information about the geometry of the realistic airway printed model. Additionally the geometry of the model is compared with the results about the geometry of real people bronchia from different research studies.

In Table A.1 the geometry of the realistic airway printed model is described by detailing length, the diameter and the angle of branching of each divergence level from the trachea, which corresponds with the generation level 0, until the 6th level of generation.

The position of the tongue is known to have a key influence on the exhalation flow emitted through the mouth [25,59]. The model used in this study corresponds to a relaxed state of the tongue with the tip touching the lower incisors of the model.

The geometry used for this study compares with the models considered in other studies. The main source of knowledge on this matter is human autopsies [85–88]. However, recently, and due to the advance of the technology, the geometrical information can be gathered from computer tomography scans imaging (CT-imaging) [89]. A comparative between the geometries considered in each case is summarized in Table A.2.

Appendix B. Convergence of individual measurements

A study has been made of the convergence of the velocity values obtained throughout the $N = 50$ trials carried out to obtain the velocity field in each of the planes considered. The point of maximum velocity in different planes and instants, $\widehat{U}$ has been considered as a representative value of the set of measurements. For this purpose, the cumulative average of the values obtained up to each one of the trials, $\bar{U}^k$ has been used, using the velocity modulus obtained in each case, U, leading to $\bar{U}^k/U$.

In order to compare the results, each measurement has been normalized using the final value obtained for the 50 tests. The results for the different planes considered are shown in Fig. B.1

It is possible to observe that from measurement $k = 20$ the values of the averages remain within $\pm 1.5\%$ of the final measurement. This is why the consideration of 50 trials for each of the measurements is considered as an acceptable value.

Table A.2
Comparative of the studied 3D printed model with the results obtained in different studies about the geometry of the respiratory bronchia. NI, Not included. NP, not provided.

Authors	Method	Oropharynx				Trachea		Main bronchi		
		Nasal cavity		Oral cavity						
		Nasal passage surface area (mm^2)	Vol (mm^3)	Mouth area (mm^2)	Vol (mm^3)	Mean length (mm)	Mean diameter (mm)	Mean length (mm)	Mean diameter (mm)	Mean first bifurcation angle (°)
Weibel [85], Model 'A'	Idealized model based on autopsy	NI	NI	NI	NI	120.0	16.0	47.6	12.2	35
Bailey [90]	Summarized data based on autopsy	15000	NP	NP	49000	91.0	16.5	38.0	12.0	36
Finlay et al. [86]	Idealized model based on autopsy and CT-imaging	NI	NI	283	52000	124.60	18.10	36.10	14.10	35.00
Zhou and Cheng [87]	Semi-realistic glass model based on autopsy	NI	NI	414	51400	74.4	15.8	35.0	19.0	35
Phuong and Ito [89]	3D-printed replica based on CT-imaging	NP	NP	NP	NP	NP	NP	NP	NP	NP
Berlanga et al. [60] and current study	3D-printed replica based on CT-imaging	24339	35318	260	33927	110.9	20.5	43.7	16.9	43.7

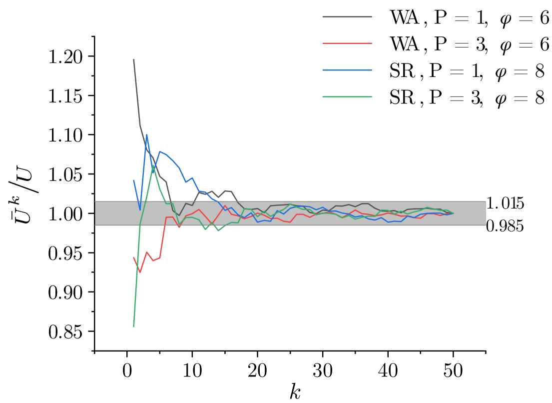

Fig. B.1. Convergence of individual trial velocity registers to their final value. Cumulative average of the values obtained up to each one of the trials, $\bar{U}^k$.

References

[1] F.B. Wurie, S.D. Lawn, H. Booth, P. Sonnenberg, A.C. Hayward, Bioaerosol production by patients with tuberculosis during normal tidal breathing: implications for transmission risk, Thorax 71 (6) (2016) 549–554, https://doi.org/10.1136/thoraxjnl-2015-207295, iSBN: 2015207295.
[2] Y. Zheng, H. Chen, M. Yao, X. Li, Bacterial pathogens were detected from human exhaled breath using a novel protocol, J. Aerosol Sci. 117 (2018) 224–234, https://doi.org/10.1016/j.jaerosci.2017.12.009.
[3] L. Liu, Y. Li, P.V. Nielsen, J. Wei, R.L. Jensen, Short-range airborne transmission of expiratory droplets between two people, Indoor Air (2016) 1–11, https://doi.org/10.1111/ina.12314.
[4] L. Morawska, Droplet fate in indoor environments, or can we prevent the spread of infection?, in: Proceedings of the Indoor Air 2005 Conference, 2005. Issue: September 2005.
[5] J.P. Duguid, The numbers and the sites of origin of the droplets expelled during expiratory activities, Edinburgh Med. J. 52 (11) (1945) 385.
[6] M. Zhou, J. Zou, A dynamical overview of droplets in the transmission of respiratory infectious diseases, Phys. Fluids 33 (3) (2021) 031301, https://doi.org/10.1063/5.0039487.
[7] C. Chao, M. Wan, L. Morawska, G. Johnson, Z. Ristovski, M. Hargreaves, K. Mengersen, S. Corbett, Y. Li, X. Xie, D. Katoshevski, Characterization of expiration air jets and droplet size distributions immediately at the mouth opening, J. Aerosol Sci. 40 (2) (2009) 122–133, https://doi.org/10.1016/j.jaerosci.2008.10.003.
[8] X. Xie, Y. Li, A.T.Y. Chwang, P.L. Ho, W.H. Seto, How far droplets can move in indoor environments - revisiting the Wells evaporation-falling curve, Indoor Air 17 (3) (2007) 211–225, https://doi.org/10.1111/j.1600-0668.2007.00469.x.
[9] J. Wang, F. Dalla Barba, A. Roccon, G. Sardina, A. Soldati, F. Picano, Modelling the direct virus exposure risk associated with respiratory events, J. R. Soc. Interface 19 (186) (2022) 20210819, https://doi.org/10.1098/rsif.2021.0819.
[10] L. Liu, J. Wei, Y. Li, A. Ooi, Evaporation and dispersion of respiratory droplets from coughing, Indoor Air 27 (1) (2017), https://doi.org/10.1111/ina.12297.
[11] R. Mittal, R. Ni, J.-H. Seo, The flow physics of COVID-19, J. Fluid Mech. 894 (2020) F2, https://doi.org/10.1017/jfm.2020.330.
[12] L. Bourouiba, E. Dehandschoewercker, J. Bush, Violent expiratory events: on coughing and sneezing, J. Fluid Mech. 745 (2014) 537–563, https://doi.org/10.1017/jfm.2014.88.
[13] L. Bourouiba, The fluid dynamics of disease transmission, Annu. Rev. Fluid Mech. 53 (1) (2021) 473–508, https://doi.org/10.1146/annurev-fluid-060220-113712.
[14] H. Wang, Z. Li, X. Zhang, L. Zhu, Y. Liu, S. Wang, The motion of respiratory droplets produced by coughing, Phys. Fluids 32 (12) (2020) 125102, https://doi.org/10.1063/5.0033849.
[15] I. Eames, J.W. Tang, Y. Li, P. Wilson, Airborne transmission of disease in hospitals, J. R. Soc. Interface 6 (Suppl 6(October)) (2009) S697–S702, https://doi.org/10.1098/rsif.2009.0407.focus.
[16] R. Tellier, Review of aerosol transmission of influenza A virus, Emerg. Infect. Dis. 12 (11) (2006) 1657, https://doi.org/10.3201/eid1211.060426, publisher: Centers for Disease Control and Prevention.
[17] J.W. Tang, W.P. Bahnfleth, P.M. Bluyssen, G. Buonanno, J.L. Jimenez, J. Kurnitski, Y. Li, S. Miller, C. Sekhar, L. Morawska, L.C. Marr, A.K. Melikov, W.W. Nazaroff, P.V. Nielsen, R. Tellier, P. Wargocki, S.J. Dancer, Dismantling myths on the airborne transmission of severe acute respiratory syndrome coronavirus-2 (SARS-CoV-2), J. Hosp. Infect. 110 (2021) 89–96, https://doi.org/10.1016/j.jhin.2020.12.022.
[18] R.M. Jones, L.M. Brosseau, Aerosol transmission of infectious disease, Indian J. Occup. Environ. Med. 57 (5) (2015) 501–508, https://doi.org/10.1097/JOM.0000000000000448.
[19] W.F. Wells, On air-borne infection. II. Droplets and droplet nuclei, Am. J. Hyg. 20 (1934) 611–618.
[20] Z.Y. Han, W.G. Weng, Q.Y. Huang, Characterizations of particle size distribution of the droplets exhaled by sneeze, J. R. Soc. Interface 10 (88) (2013) 20130560, https://doi.org/10.1098/rsif.2013.0560.
[21] T. Greenhalgh, J.L. Jimenez, K.A. Prather, Z. Tufekci, D. Fisman, R. Schooley, Ten scientific reasons in support of airborne transmission of SARS-CoV-2, Lancet 397 (10285) (2021) 1603–1605, https://doi.org/10.1016/S0140-6736(21)00869-2.
[22] L. Morawska, J. Cao, Airborne transmission of SARS-CoV-2: the world should face the reality, Environ. Int. 139 (2020) 105730, https://doi.org/10.1016/j.envint.2020.105730.
[23] C.C. Wang, K.A. Prather, J. Sznitman, J.L. Jimenez, S.S. Lakdawala, Z. Tufekci, L.C. Marr, Airborne transmission of respiratory viruses, Science 373 (6558) (2021) eabd9149, https://doi.org/10.1126/science.abd9149.
[24] M. Han, R. Ooka, H. Kikumoto, W. Oh, Y. Bu, S. Hu, Experimental measurements of airflow features and velocity distribution exhaled from sneeze and speech using particle image velocimetry, Build. Environ. 205 (2021) 108293, https://doi.org/10.1016/j.buildenv.2021.108293.
[25] E. Thacher, S.A. Mäkiharju, Effect of coherent structures on particle transport and deposition from a cough, Aerosol Sci. Technol. 56 (5) (2022) 425–433, https://doi.org/10.1080/02786826.2022.2044449.
[26] J. Wei, Y. Li, Enhanced spread of expiratory droplets by turbulence in a cough jet, Build. Environ. 93 (2015) 86–96, https://doi.org/10.1016/j.buildenv.2015.06.018.
[27] T. Dbouk, D. Drikakis, On coughing and airborne droplet transmission to humans, Phys. Fluids 32 (5) (2020) 053310, https://doi.org/10.1063/5.0011960.
[28] M. VanSciver, S. Miller, J. Hertzberg, Particle image velocimetry of human cough, Aerosol Sci. Technol. 45 (3) (2011) 415–422, https://doi.org/10.1080/02786826.2010.542785.

[29] J.K. Gupta, C.-H. Lin, Q. Chen, Characterizing exhaled airflow from breathing and talking, Indoor Air 20 (1) (2010) 31–39, https://doi.org/10.1111/j.1600-0668.2009.00623.x.

[30] P. Bahl, C. de Silva, C.R. MacIntyre, S. Bhattacharjee, A.A. Chughtai, C. Doolan, Flow dynamics of droplets expelled during sneezing, Phys. Fluids 33 (11) (2021) 111901, https://doi.org/10.1063/5.0067609.

[31] S. Asadi, A.S. Wexler, C.D. Cappa, S. Barreda, N.M. Bouvier, W.D. Ristenpart, Aerosol emission and superemission during human speech increase with voice loudness, Sci. Rep. 9 (1) (2019) 2348, https://doi.org/10.1038/s41598-019-38808-z.

[32] Z.P. Tan, L. Silwal, S.P. Bhatt, V. Raghav, Experimental characterization of speech aerosol dispersion dynamics, Sci. Rep. 11 (1) (2021) 3953, https://doi.org/10.1038/s41598-021-83298-7.

[33] V. Stadnytskyi, C.E. Bax, A. Bax, P. Anfinrud, The airborne lifetime of small speech droplets and their potential importance in SARS-CoV-2 transmission, Proc. Natl. Acad. Sci. 117 (22) (2020) 11875–11877, https://doi.org/10.1073/pnas.2006874117.

[34] J.P. Duguid, The size and the duration of air-carriage of respiratory droplets and droplet-nuclei, Epidemiol. Infect. 44 (6) (1946) 471–479, https://doi.org/10.1017/S0022172400019288.

[35] V. Stadnytskyi, P. Anfinrud, A. Bax, Breathing, speaking, coughing or sneezing: what drives transmission of SARS-CoV-2?, J. Int. Med. 290 (5) (2021) 1010–1027, https://doi.org/10.1111/joim.13326.

[36] L. Morawska, G. Johnson, Z. Ristovski, M. Hargreaves, K. Mengersen, S. Corbett, C. Chao, Y. Li, D. Katoshevski, Size distribution and sites of origin of droplets expelled from the human respiratory tract during expiratory activities, J. Aerosol Sci. 40 (3) (2009) 256–269, https://doi.org/10.1016/j.jaerosci.2008.11.002.

[37] S.A. Lauer, K.H. Grantz, Q. Bi, F.K. Jones, Q. Zheng, H.R. Meredith, A.S. Azman, N.G. Reich, J. Lessler, The incubation period of coronavirus disease 2019 (COVID-19) from publicly reported confirmed cases: estimation and application, Ann. Intern. Med. 172 (9) (2020) 577–582, https://doi.org/10.7326/M20-0504.

[38] COVID-19 Pandemic Planning Scenarios, Technical report, Centers for Disease Control and Prevention, 2021.

[39] X. He, E.H.Y. Lau, P. Wu, X. Deng, J. Wang, X. Hao, Y.C. Lau, J.Y. Wong, Y. Guan, X. Tan, X. Mo, Y. Chen, B. Liao, W. Chen, F. Hu, Q. Zhang, M. Zhong, Y. Wu, L. Zhao, F. Zhang, B.J. Cowling, F. Li, G.M. Leung, Temporal dynamics in viral shedding and transmissibility of COVID-19, Nat. Med. 26 (5) (2020) 672–675, https://doi.org/10.1038/s41591-020-0869-5.

[40] M. El Hassan, H. Assoum, N. Bukharin, H. Al Otaibi, M. Mofijur, A. Sakout, A review on the transmission of COVID-19 based on cough/sneeze/breath flows, Eur. Phys. J. Plus 137 (1) (2021) 1, https://doi.org/10.1140/epjp/s13360-021-02162-9.

[41] K. Mahjoub Mohammed Merghani, B. Sagot, E. Gehin, G. Da, C. Motzkus, A review on the applied techniques of exhaled airflow and droplets characterization, Indoor Air 31 (1) (2021) 7–25, https://doi.org/10.1111/ina.12770.

[42] W.C. Adams, Measurement of breathing rate and volume in routinely performed daily activities, Technical report, https://www.arb.ca.gov/research/apr/past/a033-205.pdf. Publication Title: California Environmental Portection Agency. Air resources board. Research division. Issue: A033-205.

[43] G.C. Leiner, S. Abramowitz, M.J. Small, V.B. Stenby, Cough peak flow rate, Am. J. Med. Sci. 251 (2) (1966) 211–214, https://doi.org/10.1097/00000441-196602000-00013.

[44] C. Xu, P.V. Nielsen, G. Gong, L. Liu, R.L. Jensen, Measuring the exhaled breath of a manikin and human subjects, Indoor Air (2014) 1–10, https://doi.org/10.1111/ina.12129, iSBN: 1397312386.

[45] J.W. Tang, A. Nicolle, C. Klettner, J. Pantelic, L. Wang, A. Suhaimi, A. Tan, G. Ong, R. Su, C. Sekhar, D. Cheong, K.W. Tham, Airflow dynamics of human jets: sneezing and breathing - potential sources of infectious aerosols, PLoS ONE 8 (4) (2013) e59970, https://doi.org/10.1371/journal.pone.0059970.

[46] H. Nishimura, S. Sakata, A. Kaga, A new methodology for studying dynamics of aerosol particles in sneeze and cough using a digital high-vision, high-speed video system and vector analyses, PLoS ONE 8 (11) (2013) 1932–6203, https://doi.org/10.1371/journal.pone.0080244, iSBN: 1932-6203.

[47] C. Xu, P.V. Nielsen, L. Liu, R.L. Jensen, G. Gong, Human exhalation characterization with the aid of schlieren imaging technique, Build. Environ. 112 (November) (2017) 190–199, https://doi.org/10.1016/j.buildenv.2016.11.032.

[48] J.W. Tang, A. Nicolle, J. Pantelic, G.C. Koh, L.D. Wang, M. Amin, C.A. Klettner, D.K.W. Cheong, C. Sekhar, K.W. Tham, Airflow dynamics of coughing in healthy human volunteers by shadowgraph imaging: an aid to aerosol infection control, PLoS ONE 7 (4) (2012) e34818, https://doi.org/10.1371/journal.pone.0034818.

[49] S. Liu, A. Novoselac, Transport of airborne particles from an unobstructed cough jet, Aerosol Sci. Technol. 48 (11) (2014) 1183–1194, https://doi.org/10.1080/02786826.2014.968655.

[50] J. Wei, Y. Li, Human cough as a two-stage jet and its role in particle transport, PLoS ONE 12 (1) (2017) 1–15, https://doi.org/10.1371/journal.pone.0169235.

[51] X. Cao, J. Liu, N. Jiang, Q. Chen, Particle image velocimetry measurement of indoor airflow field: a review of the technologies and applications, Energy Build. 69 (2014) 367–380, https://doi.org/10.1016/j.enbuild.2013.11.012.

[52] A. Etminan, Y.S. Muzychka, K. Pope, B. Nyantekyi-Kwakye, Flow visualization: state-of-the-art development of micro-particle image velocimetry, Meas. Sci. Technol. 33 (9) (2022) 092002, https://doi.org/10.1088/1361-6501/ac75b0.

[53] M. Han, R. Ooka, H. Kikumoto, W. Oh, Y. Bu, S. Hu, Measurements of exhaled airflow velocity through human coughs using particle image velocimetry, Build. Environ. 202 (2021) 108020, https://doi.org/10.1016/j.buildenv.2021.108020.

[54] S. Zhu, S. Kato, J.-H. Yang, Study on transport characteristics of saliva droplets produced by coughing in a calm indoor environment, Build. Environ. 41 (12) (2006) 1691–1702, https://doi.org/10.1016/j.buildenv.2005.06.024.

[55] S.-B. Kwon, J. Park, J. Jang, Y. Cho, D.-S. Park, C. Kim, G.-N. Bae, A. Jang, Study on the initial velocity distribution of exhaled air from coughing and speaking, Chemosphere 87 (11) (2012) 1260–1264, https://doi.org/10.1016/j.chemosphere.2012.01.032.

[56] N. Dudalski, A. Mohamed, S. Mubareka, R. Bi, C. Zhang, E. Savory, Experimental investigation of far-field human cough airflows from healthy and influenza-infected subjects, Indoor Air 30 (5) (2020) 966–977, https://doi.org/10.1111/ina.12680.

[57] D.R. Marr, I.M. Spitzer, M. Glauser, Anisotropy in the breathing zone of a thermal manikin, Exp. Fluids 44 (4) (2007) 661–673, https://doi.org/10.1007/s00348-007-0425-9.

[58] L. Feng, S. Yao, H. Sun, N. Jiang, J. Liu, TR-PIV measurement of exhaled flow using a breathing thermal manikin, Build. Environ. 94 (January 2015) 683–693, https://doi.org/10.1016/j.buildenv.2015.11.001.

[59] P. Geoghegan, C. Spence, W.H. Ho, X. Lu, M. Jermy, P. Hunter, J. Cater, Stereoscopic PIV measurement of airflow in human speech during pronunciation of fricatives, in: 16th Int Symp on Applications of Laser Techniques to Fluid Mechanics, Lisbon (Portugal), 2012.

[60] F. Berlanga, L. Liu, P.V. Nielsen, R.L. Jensen, A. Costa, I. Olmedo, M. Ruiz de Adana, Influence of the geometry of the airways on the characterization of exhalation flows. Comparison between two different airway complexity levels performing two different breathing functions, Sustain. Cities Soc. 53 (2020) 101874, https://doi.org/10.1016/j.scs.2019.101874.

[61] ASHRAE Thermal Comfort, in: ASHRAE Handbook Fundamentals 2013, ASHRAE, Atlanta, GA, 2013, pp. 9.1–9.32.

[62] C. Willert, Adaptive PIV processing based on ensemble correlation, in: 14th International Symposium on Applications of Laser Techniques to Fluid Mechanics, Lisbon (Portugal), 2008.

[63] Dynamic Studio User's Guide.

[64] J. Westerweel, Digital Particle Image Velocimetry: Theory and Application, Ph.D. thesis 1993. Publisher: Delft University Press.

[65] A.K. Prasad, R.J. Adrian, C.C. Landreth, P.W. Offutt, Effect of resolution on the speed and accuracy of particle image velocimetry interrogation, Exp. Fluids 13 (2) (1992) 105–116, https://doi.org/10.1007/BF00218156.

[66] N.J. Lawson, J. Wu, Three-dimensional particle image velocimetry: error analysis of stereoscopic techniques, Meas. Sci. Technol. 8 (8) (1997) 894, https://doi.org/10.1088/0957-0233/8/8/010.

[67] M. Raffel, C.E. Willert, F. Scarano, C.J. Kähler, S.T. Wereley, J. Kompenhans, Particle Image Velocimetry: A Practical Guide, Springer, 2018, Google-Books-ID: wk9UDwAAQBAJ.

[68] M. Raffel, C.E. Willert, F. Scarano, C.J. Kähler, S.T. Wereley, J. Kompenhans, PIV uncertainty and measurement accuracy, in: Springer (Ed.), Particle Image Velocimetry. A Practical Guide, 1 edition, Springer, 2018.
[69] D.R. Marr, T. Khan, M. Glauser, H. Higuchi, J.S. Zhang, On particle image velocimetry (PIV) measurements in the breathing zone of a thermal breathing Manikin, ASHRAE Trans. 111 (2) (2005) 299–305.
[70] F. Berlanga, I. Olmedo, M. Ruiz de Adana, Experimental analysis of the air velocity and contaminant dispersion of human exhalation flows, Indoor Air 27 (4) (2017) 803–815, https://doi.org/10.1111/ina.12357.
[71] Z. Li, G. Song, Y. Bao, Z. Gao, Stereo-PIV experiments and large eddy simulations of flow fields in stirred tanks with Rushton and curved-Blade turbines, AIChE J. 59 (10) (2013) 3986–4003, https://doi.org/10.1002/aic.14117.
[72] N. Rajatman, Turbulent Jets, Elsevier, Amsterdam, 1976.
[73] A. Hashiehbaf, G. Romano, Particle image velocimetry investigation on mixing enhancement of non-circular sharp edge nozzles, Int. J. Heat Fluid Flow 44 (2013) 208–221, https://doi.org/10.1016/j.ijheatfluidflow.2013.05.017.
[74] Q. Zhang, H. Johari, Effects of acceleration on turbulent jets, Phys. Fluids 8 (8) (1996) 2185–2195, https://doi.org/10.1063/1.868991.
[75] R. Sangras, O.C. Kwon, G.M. Faeth, Self-preserving properties of unsteady round nonbuoyant turbulent starting jets and puffs in still fluids, J. Heat Transf. 124 (3) (2002) 460–469, https://doi.org/10.1115/1.1421047.
[76] A. Falahatpisheh, A. Kheradvar, A measure of axisymmetry for vortex rings, Eur. J. Mech. B, Fluids 49 (2015) 264–271, https://doi.org/10.1016/j.euromechflu.2014.09.003.
[77] F. Huang, J. Mi, D. Li, R. Wang, Impinging performance of high-pressure water jets emitting from different nozzle orifice shapes, Geofluids 2020 (2020) e8831544, https://doi.org/10.1155/2020/8831544, publisher: Hindawi.
[78] M. El Hassan, A. Meslem, Time-resolved stereoscopic particle image velocimetry investigation of the entrainment in the near field of circular and daisy-shaped orifice jets, Phys. Fluids 22 (3) (2010) 035107, https://doi.org/10.1063/1.3358465.
[79] S. Balachandar, S. Zaleski, A. Soldati, G. Ahmadi, L. Bourouiba, Host-to-host airborne transmission as a multiphase flow problem for science-based social distance guidelines, Int. J. Multiph. Flow 132 (2020) 103439, https://doi.org/10.1016/j.ijmultiphaseflow.2020.103439.
[80] W.E. Eagle, Measuring transient entrainment rates of a confined vaporizing diesel jet, in: ILASS Americas 26th Annual Conference on Liquid Atomization and Spray Systems, Portland (OR), 2014, p. 19.
[81] D. Akhmetov, Vortex Rings, 1 edition, Springer, Berlin, 2009.
[82] J. Pallares, A. Fabregat, S. Cito, Effects of upper respiratory tract anatomy and head movement on the buoyant flow and particle dispersion generated in a violent expiratory event, J. Aerosol Sci. 166 (2022) 106052, https://doi.org/10.1016/j.jaerosci.2022.106052.
[83] J. Villafruela, I. Olmedo, M. Ruiz de Adana, C. Méndez, P.V. Nielsen, CFD analysis of the human exhalation flow using different boundary conditions and ventilation strategies, Build. Environ. 62 (2013) 191–200, https://doi.org/10.1016/j.buildenv.2013.01.022, publisher: Elsevier Ltd.
[84] N. Gao, J. Niu, Transient CFD simulation of the respiration process and inter-person exposure assessment, Build. Environ. 41 (9) (2006) 1214–1222, https://doi.org/10.1016/j.buildenv.2005.05.014.
[85] E.R. Weibel, Morphometry of the Human Lung, Springer, 1963, Google-Books-ID: sTPRmQEACAAJ.
[86] W.H. Finlay, C.F. Lange, M. King, D.P. Speert, Lung delivery of aerosolized dextran, Am. J. Respir. Crit. Care Med. 161 (1) (2000) 91–97, https://doi.org/10.1164/ajrccm.161.1.9812094.
[87] Y. Zhou, Y.-S. Cheng, Particle deposition in a cast of human tracheobronchial airways, Aerosol Sci. Technol. 39 (6) (2005) 492–500, https://doi.org/10.1080/027868291001385, publisher: Taylor & Francis _eprint.
[88] D.M. Taylor, Human respiratory tract model for radiological protection, J. Radiol. Prot. 16 (1) (1996) 013, https://doi.org/10.1088/0952-4746/16/1/013.
[89] N.L. Phuong, K. Ito, Investigation of flow pattern in upper human airway including oral and nasal inhalation by PIV and CFD, Build. Environ. 94 (2015) 504–515, https://doi.org/10.1016/j.buildenv.2015.10.002.
[90] M. Bailey, The new ICRP model for the respiratory tract, Radiat. Prot. Dosim. 53 (1–4) (1994) 107–114, https://doi.org/10.1093/rpd/53.1-4.107.